

Chemistry and IR emission of acetylene in planet-forming regions of T Tauri disks

Impact of elemental abundances and dust properties

P. Estève¹, B. Tabone¹, E. Habart¹, E. F. van Dishoeck^{2,3}, M. Vlasblom², I. Kamp⁴, A. M. Arabhavi⁴, and S. Bruderer³

¹ Université Paris-Saclay, CNRS, Institut d'Astrophysique Spatiale, 91405 Orsay, France
e-mail: pacome.esteve@universite-paris-saclay.fr

² Leiden Observatory, Leiden University, 2300 RA Leiden, Netherlands

³ Max-Planck Institut für Extraterrestrische Physik (MPE), Giessenbachstr. 1, 85748, Garching, Germany

⁴ Kapteyn Astronomical Institute, Rijksuniversiteit Groningen, Postbus 800, 9700AV Groningen, The Netherlands

Received **

ABSTRACT

Context. JWST has revealed a broad diversity of spectra, pointing toward a wide range of physical or chemical conditions in the planet-forming regions of disks (<10 au) around T Tauri stars. In particular, acetylene (C_2H_2) is widely detected, but it remains unclear whether the spread in observed line flux is due to variation of the gas-phase C/O ratio or caused by other factors.

Aims. Our goal is to explore the parameters that influence the mid-infrared (MIR) emission of C_2H_2 and H_2O , and if the spread observed in $F_{C_2H_2}/F_{H_2O}$ is tracing a variation of the C/O ratio.

Methods. Our work is based on the DALI 2D thermochemical model which self-consistently computes the thermal and chemical structure of the disk, and predicts spectra readily comparable to JWST/MIRI observations. To robustly model organics in inner disks, several improvements have been made: (1) carbon chemistry adapted for warm environments, (2) updated UV shielding treatment, and (3) mutual line overlap in the raytracing.

Results. With the model improvements, we are able to reproduce the observed C_2H_2 fluxes of T Tauri disks with a realistic disk geometry and solar C/O ratio. Our models show that C_2H_2 is bright and detectable by JWST even with a solar C/O. Its abundance is primarily set by a balance between formation initiated by CO dissociation by X-rays and destruction of carbon chains by atomic oxygen, the latter being generated by X-ray-induced destruction of H_2O and CO. The water UV shielding and hot temperatures (500-1000 K) of the inner disk also favor acetylene formation, as they prevent the destruction of carbon chains and allow overcoming activation barriers of reactions with H_2 . C_2H_2 and H_2O emissions are not only sensitive to the C/O ratio but also to the total O/H elemental abundance, supporting recent claims. In particular, we find that enhanced O/H reduces acetylene emission due to an excess of atomic oxygen. $F_{C_2H_2}/F_{H_2O}$ is thus a promising tracer of the elemental composition of inner disks. Still, the dust size distribution also plays a key role in this line flux ratio, reflecting the intrinsic link between the gas and dust components. We find that increasing the abundance of small grains relative to large grains favors C_2H_2 flux over H_2O flux. Grain depletion does not affect the $F_{C_2H_2}/F_{H_2O}$ ratio as previously suggested by observational works. A preliminary comparison with published JWST observations indicates a gas-phase C/O ratio below unity and suggests that enhanced O/H ratios may be common in T Tauri disks.

Conclusions. Thermochemical models are essential for interpreting JWST spectra of inner disks, which ultimately inform on the composition of exoplanet atmospheres. Yet, robustly estimating the C/O ratio through $F_{C_2H_2}/F_{H_2O}$ requires constraining dust properties from dust emission and better characterizing the carbon chemistry.

Key words. Astrochemistry – protoplanetary disks

1. Introduction

It has been nearly three decades since the first exoplanet was discovered (Mayor & Queloz 1995). The detection of thousands of such objects since then has revealed the remarkable diversity of planetary systems. In the next decade, this diversity will be scrutinized from a new vantage point: their atmospheric compositions thanks to space-born and ground-based cutting-edge observatories (JWST, ELT, ARIEL).

However, the starting point for planet formation is essential to make the most of these future missions and link the properties of exoplanets to their formation history. Indeed, the atmospheric composition of gas giant planets can give valuable information on their formation history (Bitsch et al. 2015; Madhusudan et al. 2016; Bitsch et al. 2022). The composition of gas and

dust that is accreted by the planet is thought to vary spatially in the protoplanetary disk, following a hierarchical structure from the different sublimation temperatures of the volatile species in the gas (Öberg et al. 2011; Ligterink et al. 2024). The elemental composition of planet atmosphere, in particular the C/O ratio, may indicate when and where the planet forms by being directly linked to the composition of the disk at that location (Cridland et al. 2019; Öberg & Bergin 2021; Schneider & Bitsch 2021; O'Donovan & Bitsch 2026). Recently, other processes that shape the elemental composition of disks have emerged: the drift of icy pebbles from the outer disk that enriches the inner disk in oxygen (Banzatti et al. 2020; Kalyaan et al. 2021; Banzatti et al. 2023; Kalyaan et al. 2023; Sellek & van Dishoeck 2025; Houge et al. 2025b; Williams et al. 2025) and sublimation or chemisputtering of carbon grains that would enrich the gaseous disk in

carbon (Booth et al. 2017; Lenzuni et al. 1995; Borderies et al. 2025; Houge et al. 2025a). All of these processes will thus have a significant impact on the elemental C/O ratio, ranging from subsolar (<0.5) to super-solar (>0.5) or even $C/O > 1$.

These scenarios have been confronted to new observations with ALMA, revealing that evolved disks harbor ubiquitous substructures showing that the radial distribution of species is far from smooth (ALMA Partnership et al. 2015; Andrews 2020; Öberg et al. 2021; Booth et al. 2024). Indeed, pressure bumps can block the pebbles that drift inwards, preventing the supply of oxygen in the inner disk (Zhu et al. 2012; Pinilla et al. 2012; Banzatti et al. 2025; Gasman et al. 2025; Temmink et al. 2025), which therefore challenges the scenarios mentioned above. However, recent theoretical works suggest that these gaps might be leaky, in particular to submicron-sized grains (Weber et al. 2018; Drążkowska et al. 2019; Stammerl et al. 2023), in line with recent observations combining ALMA and JWST data (Gasman et al. 2025). Regarding the gas content of outer disks ($r > 10$ au), ALMA observations show that they are surprisingly faint in CO, which is interpreted as a chemical conversion of CO into less volatile species, resulting in $C/O > 1$ (Miotello et al. 2017; Bergin et al. 2016; Bosman et al. 2018; Miotello et al. 2019), as well as locking up CO ice in larger bodies (Krijt et al. 2020). Together with thermochemical models, CO and C_2H proved to be good tracers of the C/O ratio in the outer disk by being widely detected (Bosman et al. 2021; Sturm et al. 2022).

Inner disks ($r < 1-5$ au) have been less studied, but *Spitzer* along with ground-based instruments (CRIRES, iSHELL, TEXES) gave interesting first results in the mid-infrared (MIR). Unlike outer disks, inner disks of T Tauri stars are oxygen-rich, with bright H_2O and OH emissions (Salyk et al. 2008; Carr & Najita 2008), revealing a potentially low C/O. Regarding the main C, O and N carriers, HCN, C_2H_2 and CO_2 (and CO) are also widely detected (Pontoppidan et al. 2010; Carr & Najita 2011). JWST is now revolutionizing the field with increased sensitivity and spectral resolution, allowing to detect new species, isotopologs and thus better constrain inner disks conditions. Slab models indicate that IR emission from 5 to 27 μm is emitted from hot, upper layers at $T \sim 300 - 800$ K, with column densities typically around $N \sim 10^{16} - 10^{19} \text{ cm}^{-2}$ (Salyk et al. 2011; Kamp et al. 2023; van Dishoeck et al. 2023; Grant et al. 2023).

Interestingly, even if T Tauri disks are dominated by water emission, C_2H_2 is systematically detected with a detection rate of 90% (Arulanantham et al. 2025; Grant et al. 2025), suggesting that this molecule might have a special place among hydrocarbons. Moreover, JWST observations of Very Low Mass Stars (VLMS) show a very rich carbon chemistry, with new detections of C_4H_2 , C_6H_6 , C_3H_4 , CH_4 , and very little water (Tabone et al. 2023; Arabhavi et al. 2024; Kanwar et al. 2024; Arabhavi et al. 2025). In particular, C_2H_2 is the most prominent feature with a pseudo-continuum reaching $N \sim 10^{22} \text{ cm}^{-2}$, reinforcing the fact that C_2H_2 is central in carbon chemistry. These results suggest that, as opposed to T Tauris, VLMS might have a high C/O ratio (Kanwar et al. 2026).

Nevertheless, Grant et al. (2025) found that the emissions of C_2H_2 and H_2O vary by 2 orders of magnitude among T Tauri disks, showing that the chemistry in inner disks is not entirely dictated by the mass of the central star. This spread possibly traces the diversity of C/O ratio in the inner disk, with C_2H_2 tracing the carbon and H_2O the oxygen. We now need thermochemical models to better understand the physical and chemical processes at stake in these regions.

Previous works on thermochemical models show that MIR emission comes from the surface of the disk atmosphere, but the

layer depends on the species, like onion layers, with at the very top CO and OH, then H_2O and CO_2 and deeper C_2H_2 and HCN (Woitke et al. 2018). However, numerous studies have shown that MIR molecular emission depends on the atmospheric conditions of the disk, including dust properties. Meijerink et al. (2009) and Glassgold et al. (2009) revealed that water emission can be significantly increased by depleting grains in the atmosphere or by flattening the dust size distribution. Antonellini et al. (2015) confirmed that dust opacity sets the water emission, expanding the dependency to the UV field and the disk geometry. More recently, Antonellini et al. (2023) claim that the trend of HCN/ H_2O with dust disk mass seen in Najita et al. (2013) can be explained by dust evolution, following the prescription of Greenwood et al. (2019a) which includes dust settling, growth and radial drift, resulting in increasing the gas-to-dust ratio and grain sizes over time.

Results concerning organic molecules, especially acetylene, are still debated, probably due to the organic chemistry being much more complex than the oxygen chemistry. Agúndez et al. (2008) predicted that the steady-state abundance of C_2H_2 and organic molecules should be higher in X-ray dominated regions, but they should decrease with more X-ray irradiation, later confirmed by Najita et al. (2011). In contrast, Woitke et al. (2024) predicted the opposite and Greenwood et al. (2019b) found no dependence of C_2H_2 on X-rays. However, most of these studies significantly underproduced acetylene (Najita et al. 2011; Woitke et al. 2018; Greenwood et al. 2019b). Kanwar et al. (2024) extended the ProDiMo chemical network DIANA (Kamp et al. 2017) to include hydrocarbons until 8 atoms of carbon, but it did not increase the emission of C_2H_2 . Woitke et al. (2024) solved the underproduction of acetylene by adopting a smooth inner rim, which enables the formation of acetylene above the optically thick dust layer in a very hot region. The column densities derived by Walsh et al. (2015) and Anderson et al. (2021) were consistent with *Spitzer*, but no detailed radiative transfer was performed. Nevertheless, they agree that the emission of water and acetylene are sensitive to the elemental abundances, and that the C/O ratio is a driver of the brightness of hydrocarbons. The line flux ratios HCN/ H_2O and C_2H_2 / H_2O were proposed to be promising tracers of the C/O ratio, allowing us to constrain the chemical composition of inner disks (Najita et al. 2011; Anderson et al. 2021). Using the same model as Woitke et al. (2024), Arabhavi et al. (2026) also did the synthetic prediction of the elemental abundances with detailed radiative transfer, but did not include water UV shielding. Indeed, Bosman et al. (2022a) and Duval et al. (2022) recently showed that water can efficiently shield the molecular layers by absorbing UV photons that photodissociate molecules. This process significantly boosts the abundance of organic molecules, which means that models do not require a high C/O ratio to produce abundant C_2H_2 .

In this paper, we explore the formation of C_2H_2 and the physical processes that can enhance its emission to match the observations, including water UV shielding. We also self-consistently predict IR emission of water and acetylene to better understand the diversity of JWST spectra of T Tauri disks and put first constraints on elemental abundances.

This paper is organized as follows. Sect. 2 details the thermochemical model DALI with several improvements for the study of inner regions of protoplanetary disks. Sect. 3 first presents the results of a fiducial model to highlight the processes shaping the water and acetylene emission, and then describes the results of a grid of models covering elemental abundances, dust properties and disk geometry. A detailed discussion on different modeling

considerations as well as a comparison with observations is proposed in Sec. 4. The main results are summarized in Sect. 5.

2. Model

This section describes the DALI model, with a focus on the processes added to the code to better model inner disks. The setup and parameters explored in this work are then summarized.

2.1. DALI model

This work is based on the 2D thermo-chemical model DALI (Bruderer et al. 2012; Bruderer 2013; Bruderer et al. 2015) to self-consistently compute H₂O and C₂H₂ emission. The code is divided in several steps. After creating a grid with the input dust and gas density structure, the first step computes the dust temperature and the dust mean intensity for each cell using a 2D Monte Carlo method. Then, the thermo-chemistry module computes iteratively the abundance of each species from a given chemical network (see Section 2.2.2), the atomic and molecular excitation, and the thermal balance of the gas to get a self-consistent gas temperature, T_{gas} , and chemical abundances. This specific step has been recently improved by including the UV shielding from molecules, especially H₂O (Bosman et al. 2022a), which has a prominent impact on molecular layers of inner disks. In this work, we further improved this step by including an extended chemical network (see Section 2.2.2) and a refined treatment of the UV shielding (see Section 2.2.1). The last step of DALI builds synthetic spectra from the radiative transfer equation. Since we want to reconstruct IR spectra including thousands of lines, we use an improved fast raytracer (Bosman et al. 2017), based on the fact that the velocity gradient along the line of sight is approximately linear (Horne & Marsh 1986). We upgraded it by including so-called line-overlap, an effect that can efficiently reduce the optically thick emission of molecules, particularly C₂H₂ (see Tabone et al. 2023).

2.2. Improvements in DALI

2.2.1. UV shielding

Atoms or molecules absorb the UV field irradiated from the star. This absorption changes the spectral shape of the radiation field and reduces its strength. As a result, a species not only protects itself by reducing its photodissociation rate (self-shielding), but also protects the other species (mutual shielding). To properly treat UV shielding, the absorption of the radiation field by all species at all wavelengths should be computed. However, cross sections, which describe the interaction of atoms and molecules with the radiative field, exhibit steep variations with very narrow features. This would require a very fine wavelength grid to sample cross sections, which is computationally prohibitive.

To reduce the computational time, we evaluate the rates of photoprocesses by using the ‘computational efficiency’ format of the Leiden Database¹ (see Appendix A for technical details). This format splits each cross section into two parts: narrow features (called ‘lines’, $\Delta\lambda < 1$ nm), and smooth variations (called ‘continuum’). With this approach, we can compute photodissociation rates with a limited wavelength grid of ~ 100 points, because the ‘lines’ are integrated thanks to their respective oscilla-

tor strength. The ‘lines’ are particularly efficient to self-shield because the peaks can be very high (around $\sigma_{\text{peak}} \sim 10^{-16} - 10^{-15}$ cm²) meaning that a column density of $N = 10^{15}$ cm⁻² is sufficient to shield the gas (reached relatively easily in inner regions of protoplanetary disks for molecules such as CO, H₂, N₂). However, since the lines are very narrow, the impact on the radiation field is limited. Thus, we only consider these lines for the self-shielding. In contrast, the continuum part of the cross section affects a broad wavelength range which allows the species not only to self-shield but also to protect other molecules. Water is a good example of efficient mutual shielding (Bethell & Bergin 2009; Ádámkóvics et al. 2014; Duval et al. 2022). We note that high column densities are required for mutual shielding ($N \sim 10^{18} - 10^{19}$ cm⁻²), so this process is only relevant for abundant molecules in protoplanetary disks.

In the previous version of DALI, self-shielding is taken into account for well-known molecules (H₂, C, N₂, CO, and isotopologues) (Miotello et al. 2014; Visser et al. 2018), and the mutual shielding is usually considered for water, although the user can choose which molecules can play a role in the attenuation of the UV flux.

Our new implementation of the UV shielding extends the self-shielding to all species in the chemical network. In case the UV cross section is not available for a species, we arbitrarily choose the cross section of $c - \text{C}_3\text{H}_2$ for the photo-reactions of this species (except for C₄H₂ for which we take C₄H cross section). This cross section should more accurately reflect the typical photodissociation rate of hydrocarbons than that of water, chosen in Bosman et al. (2018)². The calculation of the photorates in DALI relies on cross-section data from the Leiden Database (Heays et al. 2017; Hrodmarsson & van Dishoeck 2023). We added other abundant molecules in the mutual shielding, for a total of 12 species: S, Fe, H₂O, OH, CO₂, HCN, CN, C₂H₂, C₃, C₂H₄, CH₄, C₂H₆. We find that H₂O is the dominant species to mutual shield with a C/O < 1 (see Sect. 3.1.2). For C/O > 1, C₃ takes over the role of UV attenuation, followed to a lesser extent by C₂H₂, since they are both abundant and have a relatively broad UV cross section. We do not expect other molecules (for which a cross section is available) to be abundant enough to play a significant role in mutual shielding. The mutual shielding efficiency of 6 over these 12 species are shown in Appendix A.2.

2.2.2. Chemical networks

The original chemical network of Bruderer et al. (2012) was first extended to include CO isotopologue chemistry (Miotello et al. 2014), and then refined to add key molecules in the chemistry of protoplanetary disks, such as HCN or C₂H (Visser et al. 2018; Miotello et al. 2019). However, the simple hydrocarbon chemistry in Miotello et al. (2019) stopped at C₂H₃, and was tailored for outer regions of disks. Bosman et al. (2022a) built a network for inner regions, based on the RATE12 network of UMIST (McElroy et al. 2013) and added 3 body reactions from Walsh et al. (2015). This very large network (674 species and 9441 reactions) extends the carbon chemistry and has already been used for the study of hydrocarbons and organic molecules in the inner disk (Duval et al. 2022; Colmenares et al. 2024). Nevertheless, this network does not particularly focus on carbon chemistry, and significantly slows down the code. The aim of this new network is twofolds: have an accurate description of the carbon chem-

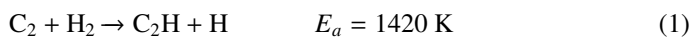
¹ https://home.strw.leidenuniv.nl/~ewine/photo/cross_sections.html

² List of hydrocarbons with $c - \text{C}_3\text{H}_2$ cross section in Appendix A.3

istry while having a simple network to avoid runtime issues³. For its construction, we start from the network of Miotello et al. (2019) and we add new species and reactions. We mainly focus on gas-phase reactions, since the emitting layers in inner disks are warm, typically $T_{\text{gas}} \sim 300 - 800$ K (Gasman et al. 2023; Grant et al. 2023; Temmink et al. 2024; Schwarz et al. 2024). This new chemical network includes 223 species and 3523 reactions, with 89 new species and 1653 new reactions. The construction follows 3 steps:

1. Select the pure hydrocarbons (C_xH_y) with 5 atoms of carbon maximum.
2. Add gas-phase reactions between these new hydrocarbons and any other species already in the network, following the types of reactions in DALI detailed in Bruderer et al. (2012). Photoreactions are included, with the updated UV cross sections from Hrodmarsson & van Dishoeck (2023) as well as the X-ray and cosmic ray induced reactions. We also add the channel of X-ray/cosmic ray induced photodissociation of H_2O leading to O which was missing in the network from Miotello et al. (2019) and in the UMIST database.
3. Add charge exchange with PAH following the prescription of Wolfire et al. (2003) as done in Bruderer et al. (2012).
4. Add adsorption/desorption for new neutral species. The binding energies are adopted from McElroy et al. (2013); Bosman et al. (2022a). When the energy is not available, we take that of the corresponding isomer. If there is no isomer, we assume a desorption energy of 3000 K (only for C_5H_5 and C_5H_6).
5. Add 3 body reactions from Bosman et al. (2022a), exported from the network of Walsh et al. (2015).

We identified several missing reactions in UMIST (RATE22 release Millar et al. 2023) compared to the KIDA database, especially reactions with high activation barriers. Many abstractions of H are missing, in particular, the key reaction with C_2 :



UMIST is tailored for cold interstellar medium (ISM) conditions, typically 10-100 K, so reactions with activation barriers of the order of 1000 K or more, are not likely to happen in dense molecular clouds. However, these reactions may have a prominent impact on the chemistry in inner regions of protoplanetary disks, with the example of water formation with $E_a = 3150$ K.

To include the reactions with high activation barriers, we combine UMIST (Millar et al. 2023) with reactions in the KIDA Database (Wakelam et al. 2024)⁴. This KIDA exportation and 'cleaning' is essentially composed of the cold ISM network from Wakelam et al. (2024) (kida.uva.2024) and extra reactions from planetology, mainly from the work of Hébrard et al. (2009) who modeled the atmospheric chemistry of Titan. The online KIDA database also contains several interesting hydrocarbon reactions from the high-temperature network of Harada et al. (2010). In addition, we include the revised endothermicities calculated by Tinacci et al. (2023). We remove all reactions with $\Delta H > 100$ kJ.mol⁻¹ (~ 12 000 K). Because of the large uncertainties of the calculated enthalpies (1200 K), we amend a reaction rate

³ This new chemical network is 10x faster (~ 31 h CPU for the chemistry of the fiducial model) than the network of Bosman et al. (2022a)

⁴ We exported the online KIDA database <https://kida.astrochem-tools.org/export/>. For this network, the exportation was done in January 2025. We included only gas-phase reactions and removed duplicated reactions, as well as reactions with rate coefficient of 0.

only when the reaction is endothermic by more than 1200 K and we adopt an activation energy equal to the enthalpy change at $T = 0$ K. Following this procedure, only 7 reactions are corrected (see Appendix B.3), including the key reaction $C_3 + H_2$. Finally, we add this KIDA network to our network by following exactly the same procedure mentioned above for UMIST.

Additionally, we include the reaction $C + H_2O \rightarrow HCO + H$ as it can be crucial for the total carbon reservoir for hydrocarbons, but not referenced in UMIST. Voitke et al. (2024) noted that this reaction is included in the online KIDA database with an unreasonable high rate, inconsistent with the upper limit in NIST Husain & Kirsch (1971) and the low temperature measurements of Hickson et al. (2016). Further details on the chosen rate are provided in Appendix B.5. This reaction reduces the acetylene emission by $\sim 30\%$.

We do not include grain surface reactions in the network, meaning that the ices are only formed via thermal adsorption, and destroyed via thermal and photo-desorption. IR active layers from which H_2O and C_2H_2 emit, are expected to be at temperatures above 300 K, so the ices do not play a major role in our study. This chemical network is therefore not suitable for studying cold regions, particularly near the midplane where ices are abundant, and surface reactions important. Finally, we do not consider the UV photolysis of carbon grains (Alata et al. 2014).

2.2.3. Line overlap

Gas-phase molecular emission lines are usually spectrally narrow. The line overlap is therefore marginal between species and even in Q -branches where thousands of lines are clustered together. However, once the lines start to be highly optically thick, they broaden and can "screen" each other significantly. In planet-forming regions, column densities of abundant species can reach $N \geq 10^{20}$ cm⁻², producing a forest of optically thick lines. As a result, neglecting line overlap can strongly overestimate the fluxes, especially in Q -branches of species such as C_2H_2 (Tabone et al. 2023). To better predict acetylene emission, we update the fast raytracer implemented in Bosman et al. (2017) to include line overlap. It reduces the Q -branch emission of C_2H_2 by a factor 1.5 for a model with a solar C/O ratio (shown in Appendix C).

2.3. Model setup

The input parameters used in this work are listed in Table 1. The 2D density structure follows a viscous accretion disk ansatz given by (Lynden-Bell & Pringle 1974):

$$\Sigma_{\text{gas}}(R) = \frac{M_D}{2\pi R_C^2} (2 - \gamma) \left(\frac{R}{R_C}\right)^{-\gamma} \exp\left[-\left(\frac{R}{R_C}\right)^{2-\gamma}\right], \quad (2)$$

with a characteristic disk radius of $R_C = 46$ au, a surface density index of $\gamma = 1.0$, and a disk mass of $M_D = 0.03 M_\odot$. The vertical distribution follows an isothermal profile :

$$\rho_{\text{gas}}(R, \theta) = \frac{\Sigma_{\text{gas}}(R)}{\sqrt{2\pi R h(R)}} \exp\left[-\frac{1}{2} \left(\frac{\pi/2 - \theta}{h(R)}\right)^2\right] \quad (3)$$

where the disk aspect ratio is given by $h(R) = h_c \left(\frac{R}{R_C}\right)^\psi$. For the fiducial model, we adopt $h_c = 0.09$ (disk aspect ratio at R_C) and

Table 1. Input parameters in DALI.

Parameter	Notation	Fiducial	Range
Mass	$M_* [M_\odot]$	1.0	-
Luminosity	$L_* [L_\odot]$	1.0	-
Effective Temp	$T_{\text{eff}} [\text{K}]$	4250	-
Accretion lum.	$L_{\text{acc}} [L_\odot]$	0.12	-
X-ray lum.	$L_X [\text{erg.s}^{-1}]$	10^{30}	$10^{27}-10^{33}$
X-ray temp.	$T_X [\text{K}]$	4.6×10^7	-
Ly- α contrib.	$Ly\alpha [L_{\text{acc}}]$	0.15	-
Disk mass	$M_D [M_\odot]$	0.03	-
Disk size	$R_{\text{out}} [\text{au}]$	10	-
Inner radius	$R_{\text{in}} [\text{au}]$	0.1	-
Critical radius	$R_c [\text{au}]$	46	-
Disk aspect ratio^a	$h_c [\text{rad}]$	0.09	0.05-0.25
Flaring angle^a	ψ	0.15	0.05-0.20
C/O	-	0.47	0.2-1.5
O/H	-	$2.9\text{e-}4$	$2.9\text{e-}5$ - $2.9\text{e-}3$
Gas-to-dust ratio^b	gd	10^3	10^2 - 10^4
Min. grain size	$a_{\text{min}} [\text{nm}]$	5	5-100
Max. grain size	$a_{\text{max}} [\text{mm}]$	1	1-100
Power law index^c	q	3.5	3.0-4.0

^(a) The disk aspect ratio here is actually a scale height angle. The flaring angle is therefore $\psi = \beta - 1$ where β is the usual flaring index defined from the scale height (in units of distance). ^(b) The gas-to-dust ratio value is vertically averaged. ^(c) Dust opacities adopted from Facchini et al. (2017).

a flaring angle of $\psi = 0.15^5$. This setup doesn't include a smooth inner rim, which could increase molecular emission, as shown in the case of EX Lupi by Woitke et al. (2024).

For this work, we use the DALI module developed by Facchini et al. (2017) to self-consistently compute the size-dependent dust settling, following Riols & Lesur (2018) and assuming a mixing parameter $\alpha = 10^{-3}$. This corresponds to the prescription used by Woitke et al. (2024), which includes the vertical dependence of the Stokes number with the gas density. For our fiducial model, the maximum grain size is $a_{\text{max}} = 1$ mm, set by fragmentation (Birnstiel et al. 2011), which is the typical regime in inner disks (Birnstiel et al. 2012; Birnstiel et al. 2015). The minimum grain size is set to $a_{\text{min}} = 5$ nm, consistent with Facchini et al. (2017). Before settling, we consider an MRN dust-size distribution (Mathis et al. 1977) with a power-law index $q = 3.5$ ($f(a) \propto a^{-q}$), consistent with the fragmentation-limited regime (Birnstiel 2024). Finally, a fiducial global gas-to-dust ratio is set to 1000, which is the typical gas-to-dust ratio achieved after 2-3 Myrs in the inner disk (Bitsch & Mah 2023). This gas-to-dust ratio is vertically averaged. Our models do not include the vertical mixing of species, although it could change the IR emission of molecules by a factor of up to 3 (Woitke et al. 2022).

The fiducial abundances are adopted from Bruderer et al. (2012) (Table B.1), consistent with Bruderer (2013); Bosman et al. (2022b). They correspond to the volatile ISM abundances based on Jonkheid et al. (2006). The C/O ratio in the fiducial model is C/O = 0.47. Hereafter, we refer to this value as the 'solar C/O' throughout the remainder of the paper, rather than 'volatile ISM C/O'. The abundances are obtained by the time-dependent solver LIMEX (Ehrig et al. 1999) with an end-time

⁵ The disk aspect ratio is defined here as a scale height angle. The corresponding flaring angle is thus defined from this scale height angle, and differs from the usual flaring index for which the scale height is in units of distance.

of 3 Myrs, which is enough to reach steady-state abundances for oxygen and carbon chemistry (Agúndez et al. 2008; Kamp et al. 2017; Kanwar et al. 2025).

Regarding the radiation field, the disk orbits a T Tauri star with an effective temperature of $T_{\text{eff}} = 4250$ K, a photospheric luminosity $L_* = 1 L_\odot$ and a mass $M_* = 1 M_\odot$. The shape of the FUV excess corresponds to a blackbody at $T = 20\,000$ K following the prescription of Tabone et al. (2024). We include a Lyman- α line with a FWHM of 200 km.s^{-1} and a total luminosity of $0.15 L_{\text{acc}}$ (Tabone et al. 2024), which contributes to $\sim 80\%$ of the FUV luminosity (Schindhelm et al. 2012; France et al. 2014). We neglect the scattering by H atoms. The X-ray spectrum is given by a blackbody at $T_X = 4.6 \times 10^7$ K between 10^3 and 10^5 eV with a luminosity of $L_X = 10^{30} \text{ erg.s}^{-1}$.

Throughout this work, the excitation of H_2O is performed in non-Local Thermal Equilibrium (non-LTE, Faure & Josselin 2008) whereas the population levels of C_2H_2 is calculated in LTE (due to a lack of collisional rate coefficients). According to Bruderer et al. (2015), the excitation of HCN and C_2H_2 should be similar. We observe a minor difference ($\sim 25\%$ reduction) in our models between LTE and non-LTE calculations for HCN thanks to infrared pumping (Bruderer et al. 2015), so non-LTE effects should not dramatically change acetylene emission.

2.4. Model grid

Throughout this work, we explore a set of input parameters to highlight the possible drivers of the acetylene emission in T Tauri disks, and its relationship with water emission. These parameters are listed in bold in Table 1. Regarding the elemental abundances, we vary the C/O ratio between 0.2 and 1.5, by keeping O/H constant and varying C/H accordingly. We also run models with 10 times more and less oxygen than the ISM to quantify the impact of an oxygen enrichment due to the drift of icy pebbles and depletion due to advection of water vapor onto the star, respectively. As with the standard grid, we vary the C/O ratio by varying C/H and keeping O/H constant. These models will be termed "enhanced O/H" and "depleted O/H" hereafter. For the disk structure, we change the disk aspect ratio from 0.05 to 0.25. The flaring angle varies from 0.05 to 0.20, but we adapt the disk aspect ratio h_c at $R_c = 46$ au to keep the same disk aspect ratio of the other models at 0.5 au. By doing so, we can better isolate the effect of the flaring angle in the inner disk.

Regarding the properties of the dust, we consider a range of gas-to-dust mass ratios, ranging from 10^2 to 10^4 . The dust size distribution is known to vary in protoplanetary disks due to vertical settling, radial drift, growth and fragmentation (Weidenschilling 1977; Brauer et al. 2008; Zsom et al. 2010; Birnstiel 2024). The minimum grain size in the inner disk is not well constrained, so we explore a large range, from 5 nm to 100 nm. This range is consistent with observation in scattered light, showing that sub-micron sized grains are present in the atmosphere of outer disks, with an upper limit of $a_{\text{min}} < 400$ nm (Tazaki & Dominik 2022). The large uncertainty on the fragmentation velocity ($v_{\text{frag}} \sim 1 - 10 \text{ m.s}^{-1}$ Blum & Wurm 2008; Güttler et al. 2010; Birnstiel et al. 2012) leads to a variation of a_{max} of a factor of 100, which is covered in this work. We also explore the impact of a different dust size distribution, since dust size distributions limited by radial drift tend to be top-heavy (Birnstiel et al. 2015; Birnstiel 2024), and SED fitting typically retrieved power-law indexes between 3 and 4 (Ribas et al. 2020; Kaeufer et al. 2023).

Finally, we explore a range of X-ray luminosity since its impact on the emission of C_2H_2 is still debated in the literature

(Najita et al. 2011; Greenwood et al. 2019b; Notsu et al. 2021; Woitke et al. 2024). This grid does not cover the effect of varying the inner disk radius since we focus only on full disks, but it could also change molecular emission as shown in Vlasblom et al. (2024).

3. Results

This section first describes the results obtained by the fiducial model (see Table 1) and explains the key processes setting the abundance of acetylene. Then, the results of the model grid are analyzed.

3.1. Fiducial model

3.1.1. Abundances and synthetic spectrum

The results of our fiducial model ($C/O = 0.47$, $gd = 10^3$, $O/H = 2.88 \times 10^{-4}$) are presented in Fig. 1. Figure 1-a shows the gas density structure, while the Fig. 1-b reveals that the dust structure is significantly different, with a strong depletion above $z/r = 0.15$ due to the dust settling. Figure 1-e shows that water is very abundant in the inner disk, in both the shielded regions inside of $r \simeq 0.6$ au and in the warm upper atmosphere extending to large radii. The formation of water is indeed greatly enhanced at high temperature to overcome the barrier to form OH (van Dishoeck et al. 2013). Water emits in this warm ($300 \text{ K} < T_{\text{gas}} < 700 \text{ K}$), upper atmosphere ($z/r > 0.15$) indicated by the red contours, which represent 80% of the emission of H_2O (water line $12_{5-8} - 11_{2-9}$, $E_u = 3273 \text{ K}$, $A = 3.84 \text{ s}^{-1}$, and $\lambda = 17.10 \mu\text{m}$). According to the panel 1-b, dust is significantly depleted where water emits, with a gas-to-dust ratio $gd \sim 5 \times 10^4$. The normalized FUV flux G_0 (Fig. 1-d) highlights the important role of H_2O in the absorption of the UV flux in inner disks. Indeed, the water distribution perfectly matches the structure of the UV field in the inner disk: when water becomes abundant, G_0 drops by orders of magnitude in a couple of cells (see Fig. 1-d and Fig. 3). It allows more complex, organic molecules to form underneath, such as acetylene (Fig. 1-f and Sec. 3.1.2).

Figure 1-f shows that C_2H_2 is present three reservoirs: the inner disk ($r < 1$ au), the upper layer of the outer disk ($r > 1$ au, $z/r > 0.20$), and near the midplane in the outer disk ($r > 1$ au, $z/r < 0.10$), consistent with other thermochemical models (Kanwar et al. 2024). Interestingly, even though $C/O = 0.47$, acetylene is particularly abundant in the first reservoir (inner disk), which will be the main focus of this paper since the IR emission seen by JWST originates from this region. Indeed, the red contours indicate that 70% of the emission of C_2H_2 (line with $E_u = 2678 \text{ K}$, $A = 5.527 \text{ s}^{-1}$ and $\lambda = 13.6872 \mu\text{m}$) is concentrated in the innermost regions of the disk, where $450 \text{ K} < T_{\text{gas}} < 1000 \text{ K}$, and $n_{\text{H}} \sim 10^{13} - 10^{14} \text{ cm}^{-3}$. These temperatures are in the typical range derived from slab model fits of the JWST spectra of T Tauri disks⁶ (Gasman et al. 2023; Grant et al. 2023; Vlasblom et al. 2025; van Dishoeck et al. 2023; Arulanantham et al. 2025). The emitting region of C_2H_2 is therefore slightly lower and closer to the star than water for lines with similar E_u , in between the UV shielded region by water and the optically thick IR layer of the dust. As acetylene emits deeper than water, the dust is less depleted where acetylene emits ($gd \sim 9 \times 10^3$) than where water emits. The H/ H_2 transition perfectly matches the layer where C_2H_2 becomes abundant, showing the crucial role of warm H_2 in its formation (see Sect. 3.1.2).

⁶ It is further discussed in Sect. 4.5

The synthetic spectrum of the fiducial model is presented in Fig. 2 between 10 and 20 μm . The continuum is typical for a T Tauri disk, with the silicate bump at 10 μm . The forest of blue lines corresponds to the water rotational lines, which is expected since the emitting region in Fig. 1-e is much higher than the dust continuum (surface $\tau_{\text{dust}}(17.10 \mu\text{m}) = 1$). Moreover, the Q-branch feature of acetylene at 13.7 μm clearly stands out, reflecting the high abundance of acetylene seen in Fig. 1-f, even though the fiducial model has a solar C/O. This is consistent with *Spitzer* and JWST observations of T Tauri disks, systematically detecting H_2O and C_2H_2 (Carr & Najita 2008, 2011; Grant et al. 2025) but in contrast with the very weak emission predicted by modeling works that neglect water UV shielding (Greenwood et al. 2019a; Kanwar et al. 2024).

3.1.2. What sets the abundance of carbon chains ?

The oxygen chemistry and, in particular, the formation and destruction pathways of H_2O have already been largely studied and understood, the main result being that water is abundant in hot, irradiated layers (Glassgold et al. 2009; Woitke et al. 2009; van Dishoeck et al. 2013; Walsh et al. 2015, $T > 300 \text{ K}$). On the other hand, the carbon chemistry is much more complex and is not yet fully understood: why is C_2H_2 so bright in T Tauri disks with a solar C/O ? This section focuses on carbon chemistry to address this question.

The formation of hydrocarbons starts from C or C^+ . The first molecule to form is carbon monoxide, CO, from C^+ and O (Fig. 3). However, with a solar C/O, there is more oxygen than carbon, so CO locks up almost all the gas-phase carbon. The oxygen left is available to form H_2O . As mentioned in previous studies discussing the formation of organic molecules, the 'free' carbon available to form hydrocarbons is released by the dissociation of CO by UV or X-rays (Bast et al. 2013; Walsh et al. 2015; Woitke et al. 2024; Kanwar et al. 2024). However, our models include the water UV shielding which suppresses the penetration of UV photons in the layer where organic molecules are abundant. This layer is actually X-ray active according to the Fig. 3. Therefore, the main production of carbon comes from the indirect dissociation of CO by X-rays, either by secondary ionization or reaction with He^+ :



Then, from this carbon released, carbon chains are built mainly from the addition of C (or C^+) and H_2 , and dissociative recombinations with electrons (Bast et al. 2013; Kanwar et al. 2024). The H-abstraction reactions often involve large activation barriers, so hydrocarbon formation is favored at high temperatures and in regions where H_2 is abundant. This explains why C_2H_2 is particularly abundant in the inner disk, just below the H/ H_2 transition, which is deeper than the C/CO transition (Fig. 3) because the warm chemistry consumes H_2 to form OH. However, X-ray induced photodissociation of CO and H_2O also releases oxygen. The latter plays an important role in the carbon chemistry by destroying carbon chains to form back CO. This channel of destruction has been overlooked so far in the literature, although Bast et al. (2013) mentioned that OH can impede the formation of carbon chains at low temperatures by the reaction $\text{C} + \text{OH} \rightarrow \text{CO} + \text{H}$. Therefore, the abundance of carbon chains and especially C_2H_2 is set by a balance between formation with

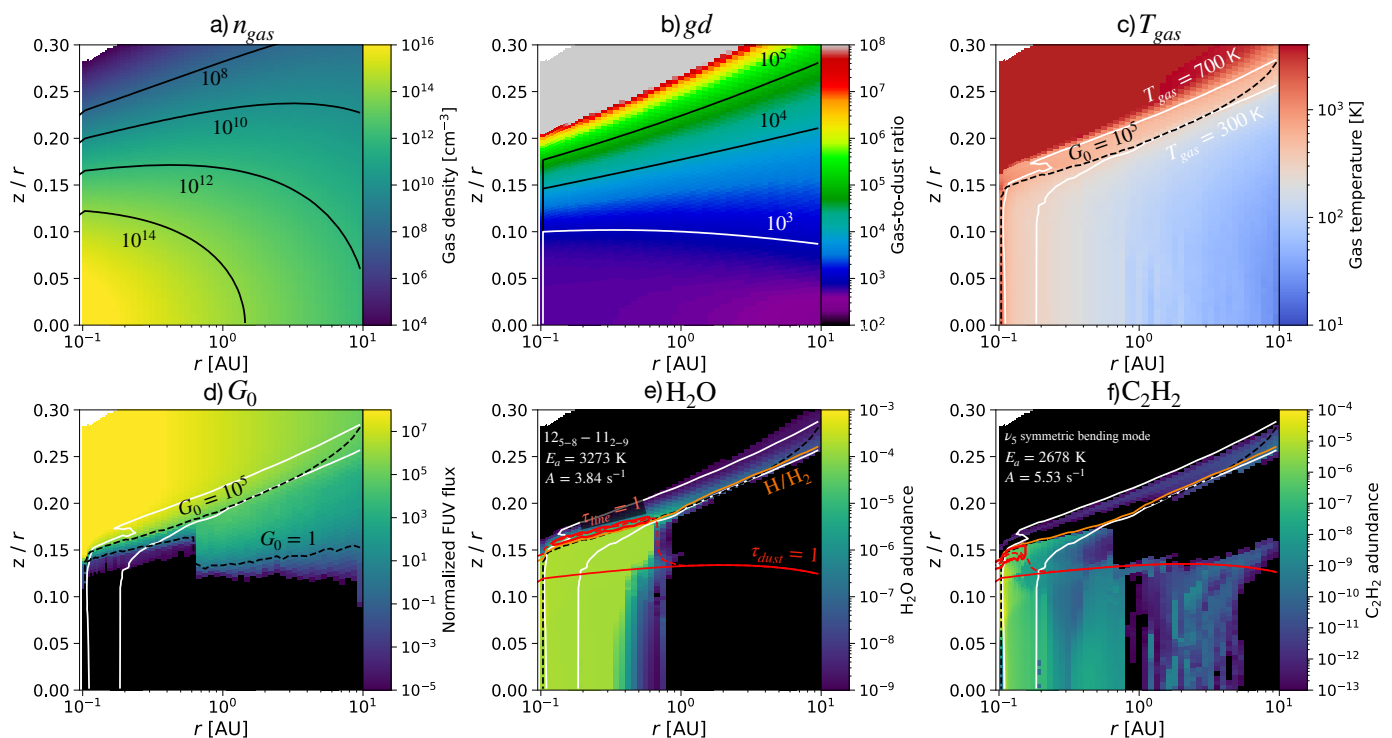


Fig. 1. Disk structure of the fiducial model. The top panels show the gas density, the local gas-to-dust ratio and the gas temperature. The bottom panels present the normalized UV field G_0 (Habing units), the abundance of H_2O and C_2H_2 . The white lines indicate the 300 K and 700 K gas temperature contours. The bottom red solid line shows the dust optically thick surface ($\tau_{\text{dust}} = 1$ at $14 \mu\text{m}$) while the dashed red line represent the surface where $\tau_{\text{line}} = 1$. The red contours correspond to 80% of the total emitting flux. The orange dashed line in the bottom panels indicate the H/H_2 transition, sometimes difficult to distinguish from the black dashed line $G_0 = 10^5$.

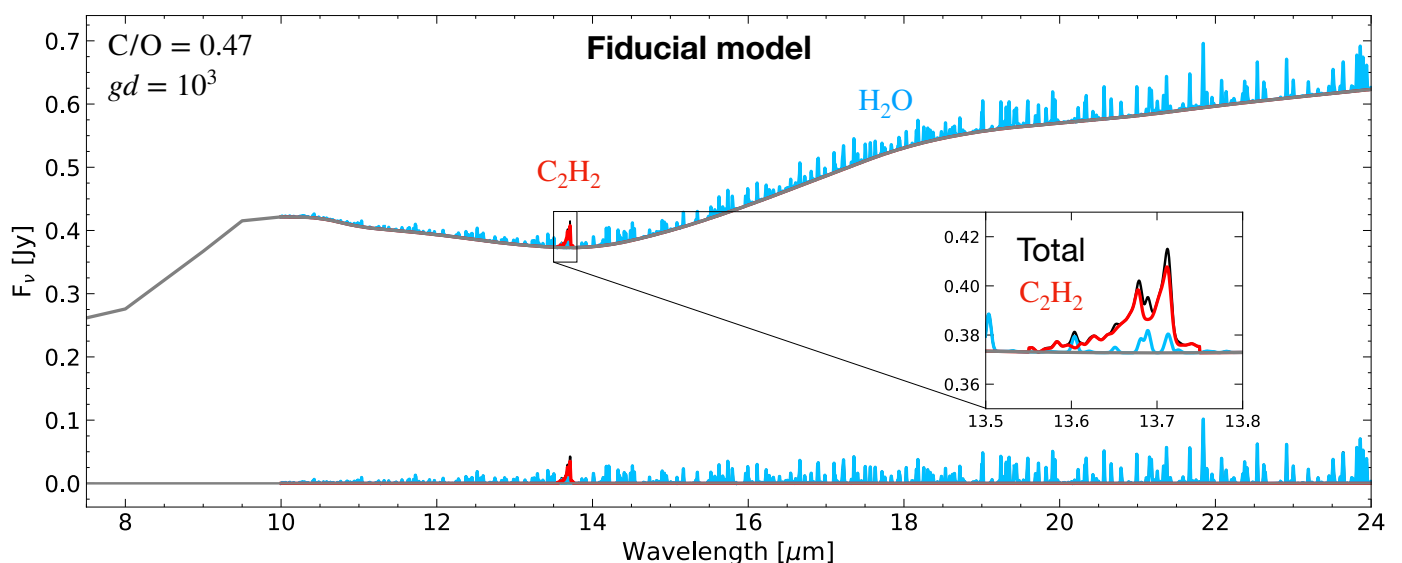


Fig. 2. DALI synthetic spectrum of C_2H_2 (red) and H_2O (blue) for the fiducial model. The total spectrum is shown in black. The spectral resolution is $\lambda/\Delta\lambda = 2000$ to mimic a JWST/MIRI spectrum. Although the fiducial model is richer in oxygen, the C_2H_2 feature stands out clearly from the forest of water lines.

the carbon released by CO dissociation, and destruction by the oxygen. This balance reveals that C_2H_2 is not expected to be sensitive to a variation of X-ray luminosity since X-rays are involved in both its formation and destruction (confirmed by Fig. E.1, with only an increase of a factor of 3 for 6 orders of magnitude in L_X). It is also crucial not to miss any reactions involving

H_2 or O or it will skew the estimation of carbon chain abundances.

Finally, Bosman et al. (2022a,b); Duval et al. (2022) strikingly showed that water UV shielding significantly enhances the abundance of organic molecules. The vertical cut at $r = 0.15$ au (Fig. 3) confirms that C_2H_2 is abundant when the water UV shielding becomes effective (represented as $G_0^{\text{H}_2\text{O shield}}$). In

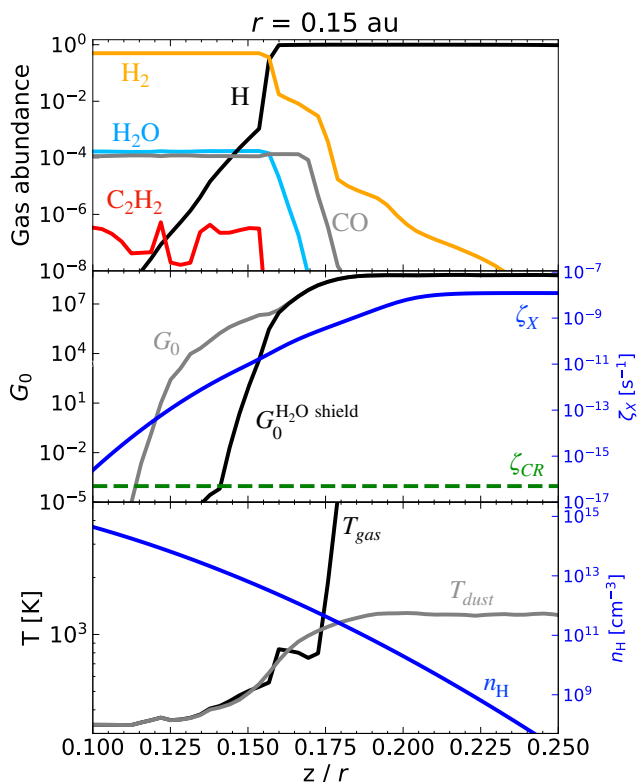


Fig. 3. Top panel: Vertical cut at $r = 0.15$ au showing the abundances of several key atoms and molecules. Middle panel: Irradiation conditions in this vertical cut, with $G_0^{\text{H}_2\text{O shield}}$ showing the UV field attenuated by water absorption (water shielding). The grey line G_0 indicates what the UV field would be without the water UV shielding. Bottom panel: Gas and dust temperature, with the gas density n_{H} in blue. Water UV shielding allows C_2H_2 to be abundant much higher in the disk by suppressing UV photodissociation.

this layer, water attenuates the UV field by 7 orders of magnitude, which suppresses the photodissociation by the UV field for species with photodissociation threshold at $\lambda \lesssim 180$ nm., helping molecules to survive. Because H_2O is no longer photodissociated, the abundance of atomic oxygen drops, quenching the destruction route of carbon chain molecules (Duval et al. 2022). It also quenches the destruction of H_2 by atomic oxygen, shifting the H/H_2 transition to higher altitudes. This leads to a higher C_2H_2 abundance in upper layers as this molecule is particularly sensitive to this transition as well (Kanwar et al. 2024). As a result, water UV shielding enhances the acetylene abundance by more than 4 orders of magnitude in the upper atmosphere (consistent with Duval et al. 2022), and it increases the emission of C_2H_2 by a factor 5 (shown in Appendix A.4). It is interesting to note that when $\text{C}/\text{O} > 1$, H_2O is much less abundant (Sect 3.2) and no longer attenuates the UV field. Instead, C_2H_2 and C_3 are the main species that shield the gas (see Appendix F).

In short, the abundance of acetylene is determined by 2 distinct processes. First, the chemistry shows that it is set by a balance between formation from atomic carbon thanks to CO dissociation by X-rays, and destruction by the atomic oxygen. Second, C_2H_2 is known to be sensitive to the UV field (Walsh et al. 2015), so suppressing UV photons with water UV shielding allows organic molecules to be abundant much higher in the disk, revealing C_2H_2 . Our model predicts an emission of C_2H_2 much brighter than other thermochemical modeling works (Woitke et al. 2018; Greenwood et al. 2019b; Kanwar et al. 2024) and

consistent with JWST observations because we enhance C_2H_2 formation by including more reactions with H_2 (see in Sec. 2.2.2 and Sec. 4) and we take into account water UV shielding.

3.2. Model grid

3.2.1. Elemental abundances

This section focuses on the impact of the elemental composition of disks on the emission of acetylene and water. To compare their emission, we followed the integration windows of Grant et al. (2025). The emission of C_2H_2 is integrated over its main Q -branch (13.6-13.72 μm) and the water emission is integrated over 3 windows: 17.09-17.15 μm , 17.2-17.245 μm , 17.3-17.45 μm . Figure 4 presents the flux of water and acetylene obtained with the grid, covering 2 parameters: C/O ratio and gas-to-dust ratio g_d . Fig. 4-a (left) shows the fiducial grid.

Increasing the C/O ratio (by increasing C/H), more carbon is available to form molecules, in particular hydrocarbons and CO. In addition, less oxygen is available to form H_2O since CO captures more oxygen as well. As a result, the water emission drops while the acetylene emission sharply increases. The C_2H_2 emission is more sensitive to the C/O ratio than H_2O , varying by a factor of 120 versus 7 respectively, between a C/O ratio of 0.2 and 1.5. Moreover, the jump seen for both molecules around C/O=1 corresponds to a switch in the chemistry. Once C/O > 1, the limiting factor becomes the oxygen. In this case, CO locks up most of the oxygen while free carbon remains: hydrocarbons and organic molecules do not need to form via the dissociation of CO, making them much more abundant (see Appendix F). This result is consistent with recent thermochemical model studies (Woitke et al. 2018; Arabhavi et al. 2026). The effect of the C/O ratio is opposite between acetylene and water: one is brighter when the other is fainter. Consequently, the line flux ratio $F_{\text{C}_2\text{H}_2}/F_{\text{H}_2\text{O}}$ is strongly dependent on the C/O ratio (Fig. 5-a), which varies by almost 3 orders of magnitude between C/O = 0.2 and C/O = 1.5. The clear jump at C/O = 1 would also allow to separate two populations of disks and may thus serve as an important observational signature.

As seen in Arabhavi et al. (2026), not only the C/O can play a role in the molecular emission, but also the total oxygen and carbon budget (O/H and C/H). With this model grid, we revisited this aspect with DALI by increasing O/H by a factor of ten compared to the standard ISM values ("enhanced O/H" models), as could be appropriate for icy grains delivering oxygen in the inner disk (see Sect. 4.6). When comparing two models with exactly the same C/O, Fig. 6 reveals how different the two spectra are. Indeed, the water lines are increased by a factor ~ 2 whereas the Q -branch of C_2H_2 drops by about the same factor. The increase in water emission is simply due to the overabundance of oxygen. As water lines are optically thick, line fluxes do not scale linearly with O/H even though its abundance is enhanced by an order of magnitude. The drop in C_2H_2 emission is, however, due to the destruction of carbon chains by oxygen. Indeed, there is more carbon released by the dissociation of CO, but also more oxygen released by CO and H_2O . The excess of oxygen released by water is then converted to CO, by depriving hydrocarbons of the available carbon. Therefore, an increase in elemental abundances pushes the balance of formation/destruction (mentioned in Section 3.1.2) towards more destruction of carbon chains, creating more oxygen-rich spectra without changing the C/O ratio. Similarly, depleting the oxygen abundance pushes this balance towards more formation of acetylene, although the effect is less pronounced due to a weaker water shielding (see the depleted

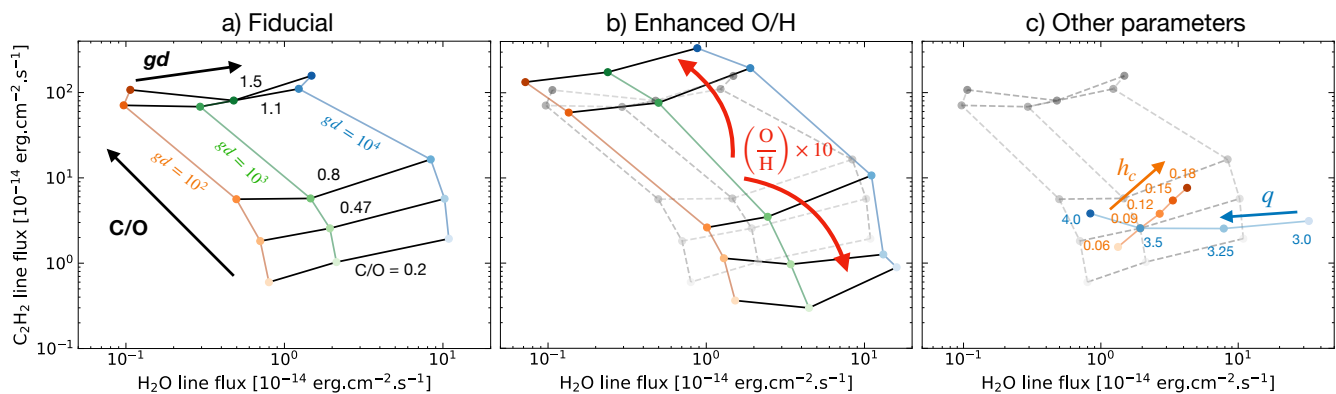


Fig. 4. Left: Result from the fiducial grid. Orange, Green and blue points correspond to $gd = 10^2, 10^3$ and 10^4 respectively. The black lines highlight a constant C/O ratio. Middle: Result obtained for the "enhanced O/H" grid: O/H $\times 10$ (C/H is scaled with the C/O ratio). The fiducial grid is overlaid in grey for reference. Right: Results for the disk aspect ratio h_c (orange), power law index of the dust distribution q (in blue) with $gd = 10^3$.

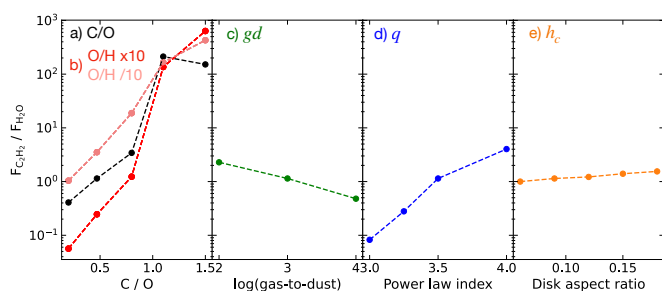


Fig. 5. Evolution of the line flux ratio C_2H_2/H_2O with the elemental abundances (C/O and O/H), gas-to-dust mass ratio gd , power law index q and disk aspect ratio h_c from left to right respectively. Fiducial model with C/O=0.47 adopted in c), d) and e) except for parameters that is varied.

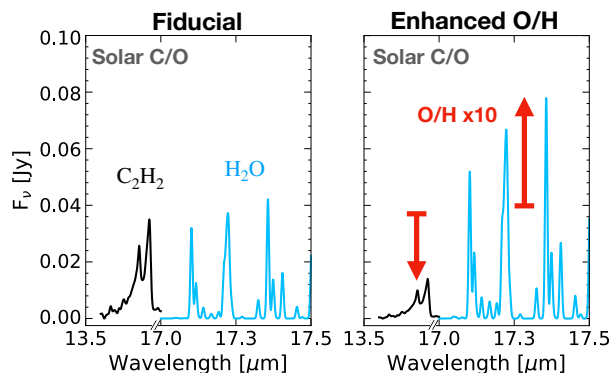


Fig. 6. DALI synthetic spectra of the fiducial model (left panel) and a model with O/H $\times 10$ (right panel). The Q -branch of C_2H_2 (black) and the water lines (blue) used for the line flux around $17.25 \mu m$ are shown together for clarity. The carbon and oxygen budget itself acts similarly to a decrease in the C/O ratio: the flux of water increases while acetylene decreases.

O/H grid in Appendix D). Our results confirm the claim of Arabhavi et al. (2026) with a different thermochemical model, reinforcing the robustness of these results.

Figure 4-b presents the results of the "enhanced O/H" grid with an increased elemental abundance of carbon and oxygen (C/H is scaled accordingly to the C/O ratio). Interestingly, the effect discussed above is only true when $C/O < 1$. When $C/O > 1$, C_2H_2 is actually brighter than with a solar O/H because the

formation of acetylene is not limited by CO. Thus, increasing the amount of carbon with a $C/O > 1$ results in more carbon chains. The flux of water decreases slightly because its formation is in competition with CO. The "depleted O/H" grid (given in Appendix D) follows the same trend but in the opposite directions.

The carbon and oxygen budget itself acts like a variation in the C/O ratio: it stretches the grid in the same direction as the C/O ratio, revealing a partial degeneracy between these two chemical parameters. According to the Fig. 5, it is still possible to differentiate between $C/O < 1$ and $C/O > 1$, but determining the exact C/O ratio requires knowledge of the O/H ratio, which can be constrained using other molecular emission lines (Arabhavi et al. 2026).

3.2.2. Dust properties

Our model grid also explores the impact of dust properties on C_2H_2 and H_2O emission. This section first describes the effect of the gas-to-dust ratio, then the parameters that fix the dust size distribution: the power law index q ($f(a) \propto a^{-q}$), the minimum and maximum grain size, a_{min} and a_{max} .

An increase in the gas-to-dust ratio (red, green and blue in Fig. 4-a) enhances all the fluxes, moving the predictions to the top right of F_{H_2O} - $F_{C_2H_2}$ plane. In fact, decreasing the gd ratio (so increasing the amount of dust) strengthens the dust continuum by increasing the total dust cross section per hydrogen atom (Facchini et al. 2017). The increased dust opacity cools the medium and pushes the line-emitting region into less dense regions, effectively reducing the emission of water and acetylene. This opacity effect is in agreement with previous modeling works on H_2O emission (Meijerink et al. 2009; Antonellini et al. 2015). However, unlike the C/O ratio, the effect of the gd ratio is the same for both water and acetylene; therefore, grain depletion does not affect $F_{C_2H_2}/F_{H_2O}$ (Fig. 5-b) as previously suggested by observational works (Tabone et al. 2023; Arabhavi et al. 2024; Grant et al. 2025).

Dust properties in the inner disks are expected to vary according to SED fitting (Ribas et al. 2020; Kaeufer et al. 2023) and theoretical works (Birnstiel et al. 2015; Birnstiel 2024). Here, we explore how the power law index q of the dust size distribution ($f(a) \propto a^{-q}$) affects molecular features in the MIR (blue in Fig. 4-c). Unlike the gas-to-dust ratio, the power-law index strongly changes the relative strength of water and acetylene emission. A flatter dust size distribution (smaller q , relatively

more large grains wrt. small grains) significantly boosts water while acetylene emission decreases slightly. This effect comes from the dust settling. Indeed, small grains are well coupled to the gas as opposed to large grains. Adopting a flatter dust distribution means that the vertical gradient of the gas-to-dust ratio would be significantly more pronounced because there are only small grains in the upper layers. As water emits vertically higher than acetylene, the contrast between water and acetylene emission is increased because the region where water emits would be much more depleted.

The minimum and maximum grain size do not appear in the right panel 4-c as they do not change the flux ratios as significantly as the power-law index (see Appendix E). By increasing the minimum grain size from 5 nm to 100 nm, UV photons penetrate deeper in the disk. Molecules are photodissociated more efficiently, pushing their emitting layers deeper. However, the IR continuum remains similar because small grains (below 100 nm) do not change the MIR opacity significantly. Consequently, C_2H_2 emission is somewhat reduced as it emits closer to the optically thick dust region. Water emission is less affected by dust continuum because it emits from slightly higher up and further out layers. Pushing its emitting region into denser layers increases its emission, similar to an increase of the gas-to-dust ratio. This effect may be different if the minimum grain size becomes larger than $0.5 \mu m$ (Woitke et al. 2016), but this is beyond the scope of this paper. Increasing the maximum grain size for a fixed gas-to-dust ratio is equivalent to increasing the gas-to-dust ratio in the upper atmosphere, because more mass is then carried by large and well-settled grains. The results shown in Appendix E confirm this behavior, with limited increase in the resulting molecular emission and a minor change in the C_2H_2/H_2O flux ratio.

3.2.3. Geometrical parameters

We finally explore the effect of the geometry on molecular emission by changing the disk aspect ratio h_c and the flaring angle ψ . When increasing the disk aspect ratio (orange in Fig. 4-c), the disk can intercept more photons from the star (the solid angle is larger), making it warmer. This extends the emitting layer of molecules, increasing their emission. In particular, C_2H_2 is more sensitive to the increase in temperature than H_2O . As a result, a thicker disk would extend the emitting layer of acetylene more than water, which is why the disk aspect ratio is more effective on acetylene than on water, with a slight increase of the line flux ratio (Fig. 5).

The effect of the flaring angle is negligible on water and acetylene emission (therefore not displayed in the Fig. 4-c). This result is in apparent contradiction with Antonellini et al. (2015); Greenwood et al. (2019b) who found that both H_2O and C_2H_2 are brighter when the disk is more flared. However, their reference points for the disk height is 0.1 and 100 au, respectively, meaning that their disk aspect ratios at 0.5 or 1 au change as well. Therefore, they likely traced the effect of disk aspect ratio rather than the flaring angle. Nevertheless, it is interesting to note that the dust continuum is significantly flatter for $\lambda \geq 15 \mu m$ when we decrease the flaring angle, even though it is not the focus of this paper.

4. Discussion

In this section, we discuss the impact of the chemical networks on C_2H_2 abundance, and explore whether other carbon

chains are expected to be abundant in this region. Then, we confront our results to JWST observations to provide first constrains on C/O and O/H in inner disks around T Tauri stars.

4.1. Chemical networks and C_2H_2

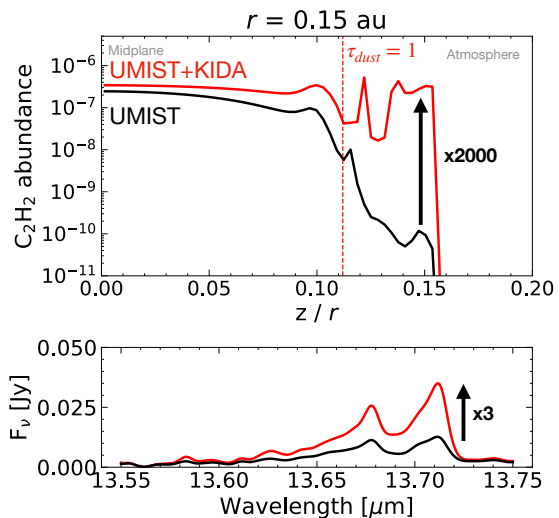


Fig. 7. Vertical cut at $r = 0.15$ au showing the abundance of C_2H_2 (top) and the corresponding spectrum (bottom) for 2 chemical networks: the fiducial (in red) and the one based on UMIST only (including also three-body reactions and $C + H_2O \rightarrow HCO + H$).

Our models are based on an extended chemical network, combining reactions from the latest version of UMIST (Millar et al. 2023, RATE22) and KIDA (Wakelam et al. 2024). This section highlights the sensitivity of C_2H_2 to chemical networks, based only on UMIST (as previous DALI networks) or on UMIST+KIDA. For this comparison, we build a network following the method described in Sec. 2.2.2 without adding reactions from KIDA (so this network also includes three-body reactions and $C + H_2O \rightarrow HCO + H$). Figure 7 presents the C_2H_2 abundance as a function of the vertical height at $r = 0.15$ AU obtained with these two chemical networks. When comparing the emitting layers (right side of the vertical red dashed line), there are more than 3 orders of magnitude difference in C_2H_2 abundance, resulting in a factor ~ 4 in C_2H_2 emission (bottom panel). This difference is mainly explained by reactions between H_2 and hydrocarbons (Appendix B.6), which are present in KIDA from the high temperature network of Harada et al. (2010), but missing in UMIST. Interestingly, Anderson et al. (2021) also used reactions from this network, and C_2H_2 was abundant in the inner disk of their heated model, which probably comes from the reactions of Harada et al. (2010). However, these reactions between carbon chains and H_2 are poorly characterized and little studied. A good example is the reaction $C_2 + H_2 \rightarrow C_2H + H$. This reaction is missing in UMIST, which might explain why Walsh et al. (2015) also do not highlight this reaction in their formation scheme of C_2H_2 . Due to a different reactivity between two closely lying electronic states of C_2 , NIST considers an activation barrier of 4000 K, inconsistent with 1420 K in Harada et al. (2010), the smaller one being the right barrier under inner disk conditions (M. van Hemert, private communication)⁷. More work has been done on the endothermicities (Tinacci et al. 2023), which enables discrimination between strongly endothermic reactions

⁷ see Appendix B.4 for more details about this inconsistency

such as $C_3 + H_2 \rightarrow C_3H + H$ (see Appendix B.3). Still, most of these reactions need to be studied to estimate the possible activation energies using quantum calculations or experimental measurements, which might ultimately change the abundances obtained with this chemical network.

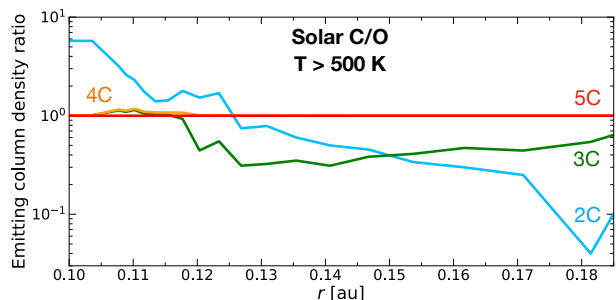
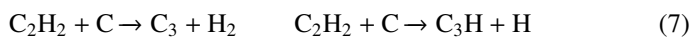


Fig. 8. Emitting column density ratio (above the surface $\tau_{\text{dust}} = 1$ at $14 \mu\text{m}$ and $T_{\text{gas}} > 500 \text{ K}$) of C_2H_2 obtained for chemical networks including various maximum number of carbon in hydrocarbons. The reference is the fiducial network including 5 atoms of carbon (5C, in red).

In addition, we examine the sensitivity of acetylene abundance to the length of carbon chains included in the chemical network. We construct 3 other networks, '2C', '3C' and '4C' with a maximum number of carbon atoms in hydrocarbons of respectively 2, 3 and 4 (the fiducial network includes hydrocarbons with a maximum of 5 carbon atoms). Figure 8 depicts the variation of the emitting column density of C_2H_2 in these 3 networks compared to our fiducial network. This sensitivity analysis shows that the network with a maximum of 4 atoms of carbon is sufficient to predict robust acetylene abundance. By extension, this would suggest that modeling the emission of an hydrocarbon with N_C atoms of carbon requires the chemical network to extend at least up to $N_C + 2$ atoms of carbon. The variation of C_2H_2 column density as a function of the length of the network is due to the successive opening of complex destruction and formation routes, which can enhance or reduce C_2H_2 abundance. For example, the 2C network underpredicts the amount of C_2H_2 outside of 0.13 au due to the reaction:



which efficiently recycles C back to CO due to the lack of an efficient route to integrate free carbon into carbon chains. In the 3C network, the reaction (6) becomes in competition with the two main reactions that lock free carbon in carbon chains (Chastaing et al. 1999; Kanwar et al. 2024):



but these reactions also destroy C_2H_2 . Therefore, the resulting abundance of C_2H_2 is not systematically higher than for the 2C network as most of the carbon is converted into C_3 (around 80%). The column density of C_2H_2 converges with the 4C network. The increase in C_2H_2 comes notably from a new formation pathway (Loison et al. 2017):



This is an example of a loop which sustains C_2H_2 even if we increase the number of carbon in species of the network. It also reveals the central place of acetylene in carbon chemistry, making it particularly abundant in warm layers of inner disks.

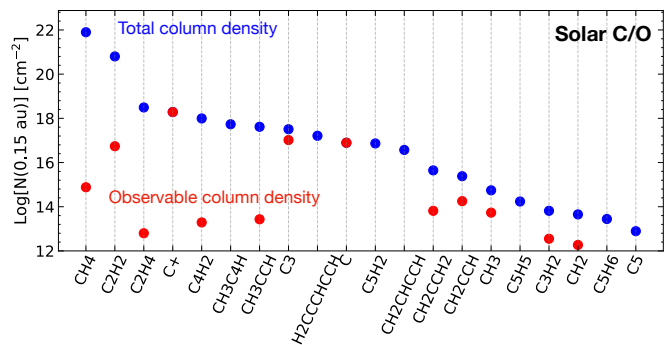


Fig. 9. Vertical column densities at $r = 0.15 \text{ au}$ for hydrocarbons. The total vertical column density is shown in blue. The red dots represent the emitting column density (above the surface $\tau_{\text{dust}} = 1$ at $14 \mu\text{m}$ and $T_{\text{gas}} > 500 \text{ K}$). While CH_4 is the major hydrocarbon, C_2H_2 is dominant in the emitting layers.

4.2. Hydrocarbons beyond acetylene

C_2H_2 is detected in nearly all disks around T Tauri, according to *Spitzer* (Pontoppidan et al. 2010) and JWST observations (Arulanantham et al. 2025; Grant et al. 2025). However, the other hydrocarbons have not been detected so far in T Tauri disks, except C_4H_2 recently (Colmenares et al. 2024). Here, we propose a broader view of hydrocarbons to try to understand why species other than C_2H_2 are hardly detectable. With a solar C/O, Fig. 9 shows that most of the free carbon is contained in methane and acetylene (total column density in blue), which clearly stand out compared to the other species. Interestingly, the emitting column density of methane is orders of magnitude smaller than C_2H_2 (red dots): most of the methane is hidden in deep layers of the disk, whereas acetylene is very abundant in upper and warm layers of the disk (see the abundance map Fig. 1). This may explain why methane is hardly detectable (non detections listed in Temmink et al. 2025 as example) while C_2H_2 is bright in disks around T Tauri.

Regarding the other hydrocarbons, C_3 is surprisingly abundant in emissive layers, although never detected so far in disks (difficult to detect in the MIR because of its main feature overlapping with CO at $4.7 \mu\text{m}$). Next, C_4H_2 has a relatively high emitting column density and has been detected for the first time around a surprisingly carbon-rich T Tauri disk in Colmenares et al. (2024). However, the two isomers of C_3H_4 (CH_2CCH_2 and CH_3CCH) have roughly the same emitting column densities as C_4H_2 but have never been observed by JWST around T Tauri stars, possibly due to a unfavorable spectroscopy compared to C_4H_2 . Interestingly, these are the same hydrocarbons that have been recently detected for the first time around Very Low Mass Stars (Tabone et al. 2023; Arabhavi et al. 2024) and brown dwarfs (Arabhavi et al. 2025; Morales-Calderón et al. 2025). Their greater stability compared to other hydrocarbons prevents them from reacting with H_2 , which may explain their abundance in the emitting layers. Given that the cross sections for most of these species are not known, the exact emitting column densities should be interpreted with caution. They strongly depend on the shape of the UV cross section, especially for $\lambda > 180 \text{ nm}$ where UV photons are not absorbed by water. Adopting the water cross-section for these species increases their emitting column density by an order of magnitude as their photodissociation is suppressed by water UV shielding, but it does not favor long carbon chains.

4.3. Dust settling prescriptions

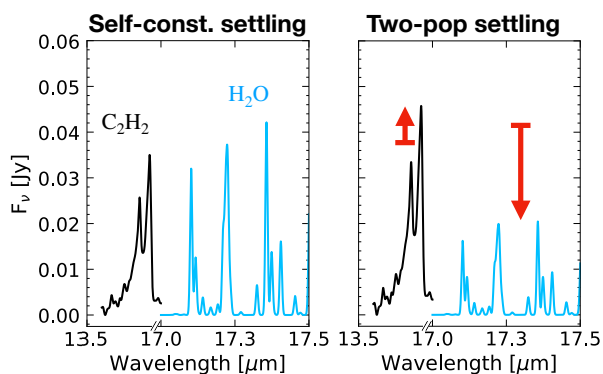


Fig. 10. DALI synthetic spectra for two dust settling prescriptions. Left: fiducial spectrum with self-consistent dust settling (Riols settling, Riols & Lesur 2018). Right: spectrum obtained with the two-pop settling prescription, based on two dust population (small - large). The two-pop settling reduces water emission by a factor 2.

Our results show that molecular emissions are sensitive to dust properties. Therefore, a_{min} , a_{max} or q defining the dust distribution prove to be important parameters to consider for the emission of acetylene and water. Another modeling consideration that could change the dust distribution is the prescription of the dust settling. So far, we used a self-consistent dust settling, following Riols & Lesur (2018) (denoted as Riols settling hereafter). We explore here if the standard DALI prescription (called "two-pop settling" hereafter, as reference to the two populations of grains considered) would change the results. In this prescription, dust is modeled by 2 components: small grains (5 nm - 1 μ m) and large grains (5 μ m - 1 mm) (following D'Alessio et al. 2006, consistent with Andrews et al. 2011) with the same composition (mixture of 60% silicate and 40% graphite, Weingartner & Draine 2001). The scale height for the small population is set to h (the same as the gas), while the scale height of large grains is reduced to χh , with $\chi = 0.2$. As for Riols settling, we consider a gas-to-dust mass ratio of $gd = 10^3$ with a fraction of large grains over small grains, $f_{large/small} = 0.90$. It corresponds to $gd = 10^4$ in the surface layers, consistent with the gas-to-dust ratio where H₂O and C₂H₂ emit (see Fig. 1-b).

Fig. 10 shows the two spectra obtained with these two prescriptions, focusing on the Q -branch of acetylene and water lines around 17 μ m. The two-pop settling underpredicts water emission by a factor of 2 compared to Riols settling, whereas the acetylene remains almost the same, with a slight increase. This different behavior arises from the two distinct line-emitting regions of these molecules. As mentioned in Sect. 3.1.1, the gas-to-dust ratio is lower where C₂H₂ emits ($gd \sim 9 \times 10^3$) than where water emits ($gd \sim 5 \times 10^4$). We also show that molecular emission is increased when the grains are depleted (see Section 3.2). Consequently, the gas-to-dust ratio of 10^4 in the upper layers of the two-pop settling model would reduce the emission of water, since the gas-to-dust ratio is locally lower (there is more dust) than in the Riols settling prescription. In contrast, where C₂H₂ emits, the difference in the gas-to-dust ratio is small, hence this increase is negligible. Extending this result to other species, since the gradient of the gas-to-dust ratio is very strong in the IR emitting layers, we expect that the two-pop settling would reduce the emission of species with higher line formation regions, such as OH, CO or H₂O, but should increase or have a negligible

impact on species emitting from deeper layers. Future studies are needed to confirm this.

4.4. Comparison with observation

The comparison of the model grid with observations from the MIRI Mid-INfrared Disk Survey (MINDS) GTO program (PID: 1282, PI: T. Henning; see Henning et al. 2024) and DoAr 33 (Colmenares et al. 2024) is shown in Figure 11. For this comparison, we select only the disks with similar characteristics as the DALI models (full T Tauri disks orbiting a star of luminosity close to solar). We export the line flux from Grant et al. (2025). The ten selected disks span over an appreciable range of luminosities (0.41 - 1.9 L_{\odot}) so we plot the line-to-continuum ratio instead of the absolute fluxes to free ourselves from this dependency. The line-to-continuum ratios are calculated with the same method as Grant et al. (2025), by dividing the peak flux of C₂H₂ (Q -branch) and H₂O (between 17.3514 μ m and 17.36 μ m) by the continuum flux at the same wavelength. We refer to Grant et al. (2025) for further information on these disks.

The fiducial grid is presented in Fig. 11-a. The absolute fluxes of C₂H₂ and H₂O predicted by DALI are in line with the observations. Our fiducial model (with solar C/O and O/H, $gd = 10^3$) reproduces disks with relatively strong C₂H₂, in between Sz 50 and DL Tau. The enhanced O/H grid (Fig. 11-b) covers most of the JWST observations, indicating that the oxygen enrichment seems to be a common feature in T Tauri disks. Fig. 11-c also suggests T Tauri disks showing the strongest water emission (wrt. to the continuum) might experience grain growth, possibly combined with a stronger settling leading to a depleted atmosphere, like XX Cha or DR Tau. Again, this underscores the importance of dust in interpreting gas emission. Interestingly, the region with $C/O > 1$ is always empty regardless of which parameter we take. Even disks showing the strongest C₂H₂ emission, like V1094Sco or DoAr33 (Colmenares et al. 2024) are not in this region. This might be evidence that T Tauri disks with a $C/O > 1$ are rare, consistent with evolutionary models by Mah et al. (2023); Sellek & van Dishoeck (2025). This result is also consistent with the ProDiMo results from Arabhavi et al. (2026), in which the region with $C/O > 1$ is orders of magnitude away from the observations.

Our models also reproduce the observed line flux ratio C₂H₂/H₂O (Fig. 12). This figure clearly shows that the spread seen in observations (Grant et al. 2025) can be explained by either the elemental abundances (C/O and O/H) or the power law index of the dust size distribution q , while gd and h_c having a negligible impact. However, as mentioned above, $C/O > 1$ clearly overshoots this spread, reinforcing that T Tauri disks are likely to have a C/O below 1 in their inner regions.

4.5. Retrieved excitation conditions

In this section, we investigate the consistency between the results of DALI and the 0D slab retrievals used to interpret JWST observations (see code and fitting procedure in Tabone et al. 2023). Figure 13 shows that the excitation conditions retrieved for C₂H₂ on DALI for a solar C/O using slab models (red crosses, $T_{ex} \sim 500$ K and effective radius corresponding to an emitting area πR^2 of $R \sim 0.1$ au) are consistent with the temperature and effective radius retrieved from JWST observations of GW Lup and DoAr 33 (Grant et al. 2023; Colmenares et al. 2024). Our thermochemical model is able to reproduce both the line flux and the excitation conditions of the C₂H₂ observed in

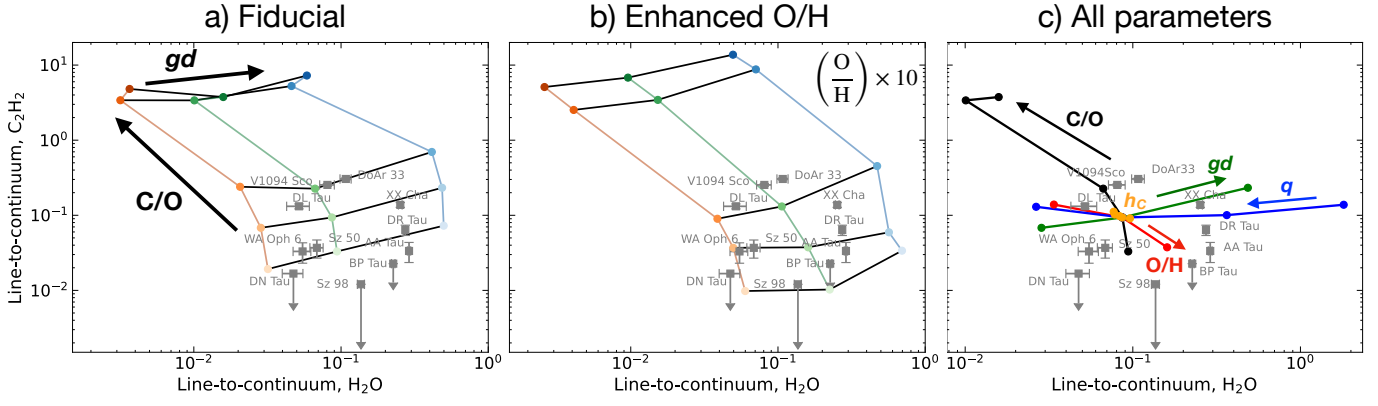


Fig. 11. Same as Fig. 4 but showing the line-to-continuum ratios for acetylene and water. The panel c) summarizes the influence of the parameters covered in this work, highlighted in colors: black for C/O, red for O/H, green for gd , blue for q and orange for hc . MINDS observations are shown with grey squares, with fluxes exported from Grant et al. (2025). We include only T Tauri full disks, without cavities. This plot suggests that a C/O > 1 is excluded in T Tauri disks, and most of the disks are better reproduced by a high O/H or low C/O.

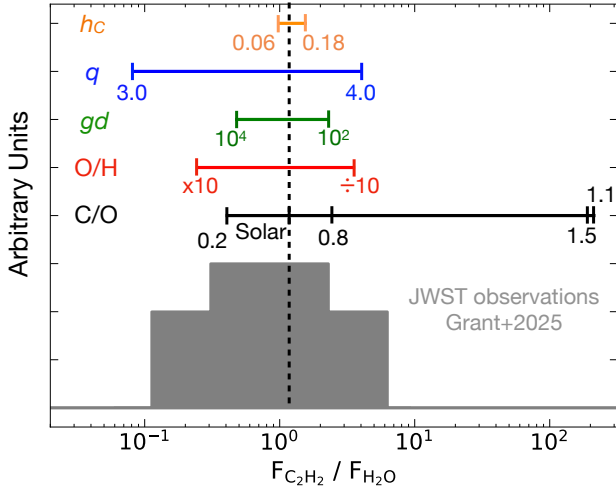


Fig. 12. Distribution of the line flux ratio C_2H_2/H_2O observed by JWST (Grant et al. 2025) compared to the parameters explored in this work. Three parameters stand out to explain this spread: C/O, O/H or q . A C/O > 1 seems excluded for inner disks of T Tauri stars.

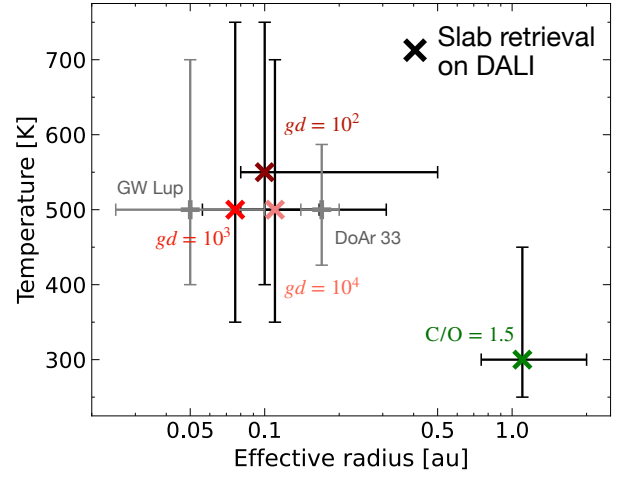


Fig. 13. Temperature and effective radius (corresponding to an emitting area πR^2) of C_2H_2 emission retrieved from slab models on DALI predicted spectra. Red crosses indicate DALI models with solar C/O and $gd = 10^2, 10^3, 10^4$, while the green cross corresponds to C/O = 1.5 and $gd = 10^3$. JWST observations of 2 disks are shown in grey (Grant et al. 2023; Colmenares et al. 2024).

disks. Figure 13 also suggests that the effective radii and temperatures do not change significantly with the gas-to-dust ratio. Interestingly, despite the large uncertainties, the conditions retrieved from the DALI model with C/O = 1.5 are distinctly colder ($T_{\text{ex}} \sim 300$ K) and more extended ($R \sim 1.1$ au), confirming that the chemical structure changes drastically when C/O > 1. This is also reflected in the abundance map of acetylene for a C/O > 1, which is dramatically different from C/O < 1 (shown in Appendix F). Our models predict that DoAr33 is one of the richest T Tauri disk in carbon C/O ~ 0.9 according to Fig. 11 with a large gas-to-dust ratio. However, the detailed analysis of DoAr 33 by Colmenares et al. (2024) determined a C/O ratio between 2-4. This difference probably arises from the chemical network: their network is based on UMIST only which underproduces acetylene (see Fig. 7) compared to our network. To compensate, they likely need to increase the C/O ratio. In addition, our study relies on molecular fluxes, whereas they compared the predicted column densities to those retrieved from single-zone slab models. Radiative transfer effects can play a role, especially in the enhanced C/O models where C_2H_2 and dust are optically

thick in the inner disk. Detailed radiative transfer is therefore needed to obtain a robust estimate of elemental abundances.

4.6. Evidence of radial drift ?

The comparison of our model grid with JWST observations suggests that most of the inner disks of T Tauri have a solar or subsolar C/O ratio, and possibly combined with an increase of elemental oxygen O/H. These two conditions are not contradictory and can be naturally fulfilled by the radial dust drift. Transport models show that oxygen-dominated ices (CO, CO_2 , H_2O) carried by grains coming from the outer disk would sublimate in the inner disk and enrich the gas phase in oxygen (Krijt et al. 2016; Booth et al. 2017; Kalyaan et al. 2021; Houge et al. 2025b). This increase of the gas-phase O/H would therefore lower the C/O ratio of the inner disk (Öberg et al. 2011, 2021; Mah et al. 2023; Sellek et al. 2025; Williams et al. 2025). As a result, water emission would increase dramatically at the expense of C_2H_2

and other organic species, the latter being destroyed in greater quantity. These results were further supported observationally by Banzatti et al. (2020, 2023, 2025). However, ALMA reveals that most disks show substructures with rings and gaps (Andrews et al. 2018). In the case of deep gaps in the disk, this drift would stop, preventing the grains from enriching the gas in oxygen. According to hydrodynamic simulations (Lubow & D’Angelo 2006; Bergez-Casalou et al. 2020), the gas from the outer disk would still cross the gap. This would elevate the C/O ratio while reducing O/H of the inner disk, since the gas from the outer disk is known to be oxygen-poor and have a high C/O ratio (Bergin et al. 2016; Miotello et al. 2017; Sturm et al. 2022). For this situation, according to our models, MIR spectra would show a prominent Q -branch of acetylene with a reduced water emission. Nevertheless, several studies did not necessarily find a relation between the substructures seen with ALMA and the molecular features of the inner disk (Gasman et al. 2025; Temmink et al. 2025), revealing that this interpretation might be too simplistic. Indeed, micron-size grains can still cross gaps and reach the inner disk (Rice et al. 2006; Zhu et al. 2012; Weber et al. 2018; Stammer et al. 2023). This would suggest that it might be the leakiness of gaps that governs the balance between the drift of dust and gas (Krijt et al. 2025), thus setting the elemental abundances in the inner disk (Tabone et al. 2026).

Following this scenario, the spread of the line flux ratio C_2H_2/H_2O might be a consequence of a change in elemental abundances due to the diversity of leakiness of gaps during the radial drift. Consequently, constraining the elemental abundances of the inner disk is fundamental to understanding the relation between inner and outer disks.

5. Conclusion

The James Webb Space Telescope is revolutionizing the characterization of the gas content in the inner disk of T Tauri stars. Our work aims to model the MIR emission of water and acetylene, two molecules ubiquitously detected by JWST, to quantify the underlying information they contain about this region. To better model inner disks, we improve the thermochemical model DALI by extending the chemical network, refining the UV self-shielding of molecules and including the line overlap in the raytracing. With a realistic disk geometry and a solar C/O ratio, we are able to reproduce the observed C_2H_2 emission in T Tauri disks reasonably well. We explore parameters related to the elemental abundances, the dust properties, and the geometry to conclude that:

- The abundance of hydrocarbons for $C/O < 1$ is set by a balance between formation seeded by CO X-ray induced dissociation and destruction by atomic O. Therefore, a change in these abundances, in particular O/H, strongly influences this balance. C_2H_2 is the most abundant hydrocarbon in emitting layers because it is a small and stable molecule, especially against reactions with H_2 , and also faster to form compared to CH_4 . It is also a key molecule in carbon chemistry as it is the intermediate to form long carbon chains.
- Our models predict observable C_2H_2 for $C/O < 1$ thanks to water UV shielding and our new chemical network, which includes many reactions between hydrocarbons and H_2 , both increasing the emission of acetylene.
- The emission of C_2H_2 and H_2O are good tracers of the elemental composition of disks. They both vary strongly with

the C/O and the O/H ratios. In particular, enhanced elemental abundances reduce C_2H_2 emission due to the excess of atomic oxygen, which destroys carbon chains.

- Dust properties also have a significant impact on molecular features. A shallower dust size distribution (lower power law index q) increases water emission but decreases acetylene emission, which can thus be a key parameter in the C_2H_2/H_2O line flux ratio. Depleting grains in the atmosphere increases both C_2H_2 and H_2O emissions, and does not favor C_2H_2 as speculated in recent observational works (in the limit of the parameter space explored).
- The spread of the line flux ratio C_2H_2/H_2O observed in T Tauri disks naturally arises from the elemental abundances (C/O and O/H), or from the dust size distribution. This highlights the importance of considering both gas and dust emission when interpreting JWST data. It also underscores the benefit of combining JWST data with inner disk dust observations to better constrain dust properties and thereby the elemental composition of the gas. Still, $C/O > 1$ is excluded to explain JWST observation, even for the disks showing a prominent C_2H_2 feature. Distinguishing between a low C/O or enhanced O/H with only C_2H_2/H_2O seems difficult, but other species such as CO_2 could help break the degeneracy according to Arabhavi et al. (2026).

The results of the model grid suggest that the gas in the inner disk of T Tauri has enhanced elemental abundances, with a $C/O < 1$, consistent with recent work (Mah et al. 2023; Sellek & van Dishoeck 2025; Tabone et al. 2026). JWST is now revealing the chemical composition of the atmospheres of close-in gas giant exoplanets, for which the C/O ratio and the metallicities appear to be in agreement with these results. A more detailed comparison and population analysis should be carried out to confirm this tentative link between disk and exoplanet composition. We finally stress that the estimates of the elemental composition of inner disks hinge on our knowledge of rate coefficients of gas-phase reactions at high temperature, which remain poorly studied for specific but yet key types of reaction, like the hydrogenation of hydrocarbons by H_2 .

Acknowledgements. The authors thank the referee for a constructive report that improved the quality of the paper. P.E and B.T thank E. Roueff, M. van Hemert, and G. Pineau des Forêts for helping us clarify the C_2+H_2 reaction rates and V. Wakelam for her support on the use of KIDA networks, and S. Facchini for his useful help with the dust settling module in DALI. P.E. and B.T also thank M. J. Colmenares for providing us the spectrum of DoAr33 and for interesting discussions regarding chemical networks.

References

- Ádámkóvics, M., Glassgold, A. E., & Najita, J. R. 2014, *ApJ*, 786, 135
 Agúndez, M., Cernicharo, J., & Goicoechea, J. R. 2008, *A&A*, 483, 831
 Alata, I., Cruz-Díaz, G. A., Muñoz Caro, G. M., & Dartois, E. 2014, *A&A*, 569, A119
 ALMA Partnership, Brogan, C. L., Pérez, L. M., et al. 2015, *ApJ*, 808, L3
 Anderson, D. E., Blake, G. A., Cleeves, L. I., et al. 2021, *ApJ*, 909, 55
 Andrews, S. M. 2020, *ARA&A*, 58, 483
 Andrews, S. M., Huang, J., Pérez, L. M., et al. 2018, *ApJ*, 869, L41
 Andrews, S. M., Wilner, D. J., Espaillat, C., et al. 2011, *ApJ*, 732, 42
 Antonellini, S., Kamp, I., Riviere-Marichalar, P., et al. 2015, *A&A*, 582, A105
 Antonellini, S., Kamp, I., & Waters, L. B. F. M. 2023, *A&A*, 672, A92
 Arabhavi, A. M., Kamp, I., Henning, T., et al. 2024, *Science*, 384, 1086
 Arabhavi, A. M., Kamp, I., Henning, T., et al. 2025, *A&A*, 699, A194
 Arabhavi, A. M., Kamp, I., van Dishoeck, E. F., et al. 2026, *A&A*, 708, A82
 Arulanantham, N., Salyk, C., Pontoppidan, K., et al. 2025, *AJ*, 170, 67
 Banzatti, A., Pascucci, I., Bosman, A. D., et al. 2020, *ApJ*, 903, 124
 Banzatti, A., Pontoppidan, K. M., Carr, J. S., et al. 2023, *ApJ*, 957, L22
 Banzatti, A., Salyk, C., Pontoppidan, K. M., et al. 2025, *AJ*, 169, 165

- Bast, J. E., Lahuis, F., van Dishoeck, E. F., & Tielsens, A. G. G. M. 2013, *A&A*, 551, A118
- Bergez-Casalou, C., Bitsch, B., Pierens, A., Crida, A., & Raymond, S. N. 2020, *A&A*, 643, A133
- Bergin, E. A., Du, F., Cleeves, L. I., et al. 2016, *ApJ*, 831, 101
- Bethell, T. & Bergin, E. 2009, *Science*, 326, 1675
- Birnstiel, T. 2024, *ARA&A*, 62, 157
- Birnstiel, T., Andrews, S. M., Pinilla, P., & Kama, M. 2015, *ApJ*, 813, L14
- Birnstiel, T., Klahr, H., & Ercolano, B. 2012, *A&A*, 539, A148
- Birnstiel, T., Ormel, C. W., & Dullemond, C. P. 2011, *A&A*, 525, A11
- Bitsch, B., Lambrechts, M., & Johansen, A. 2015, *A&A*, 582, A112
- Bitsch, B. & Mah, J. 2023, *A&A*, 679, A11
- Bitsch, B., Schneider, A. D., & Kreidberg, L. 2022, *A&A*, 665, A138
- Blum, J. & Wurm, G. 2008, *ARA&A*, 46, 21
- Booth, A. S., Leemker, M., van Dishoeck, E. F., et al. 2024, *AJ*, 167, 164
- Booth, R. A., Clarke, C. J., Madhusudhan, N., & Ilee, J. D. 2017, *MNRAS*, 469, 3994
- Borderies, A., Commerçon, B., & Bourdon, B. 2025, *A&A*, 694, A89
- Bosman, A. D., Alarcón, F., Bergin, E. A., et al. 2021, *ApJS*, 257, 7
- Bosman, A. D., Bergin, E. A., Calahan, J., & Duval, S. E. 2022a, *ApJ*, 930, L26
- Bosman, A. D., Bergin, E. A., Calahan, J. K., & Duval, S. E. 2022b, *ApJ*, 933, L40
- Bosman, A. D., Bruderer, S., & van Dishoeck, E. F. 2017, *A&A*, 601, A36
- Bosman, A. D., Walsh, C., & van Dishoeck, E. F. 2018, *A&A*, 618, A182
- Brauer, F., Dullemond, C. P., & Henning, T. 2008, *A&A*, 480, 859
- Bruderer, S. 2013, *A&A*, 559, A46
- Bruderer, S., Harsono, D., & van Dishoeck, E. F. 2015, *A&A*, 575, A94
- Bruderer, S., van Dishoeck, E. F., Doty, S. D., & Herczeg, G. J. 2012, *A&A*, 541, A91
- Carr, J. S. & Najita, J. R. 2008, *Science*, 319, 1504
- Carr, J. S. & Najita, J. R. 2011, *ApJ*, 733, 102
- Chastaing, D., James, P. L., Sims, I. R., & Smith, I. W. M. 1999, *Physical Chemistry Chemical Physics (Incorporating Faraday Transactions)*, 1, 2247
- Colmenares, M. J., Bergin, E. A., Salyk, C., et al. 2024, *ApJ*, 977, 173
- Cridland, A. J., Eistrup, C., & van Dishoeck, E. F. 2019, *A&A*, 627, A127
- D'Alessio, P., Calvet, N., Hartmann, L., Franco-Hernández, R., & Servín, H. 2006, *ApJ*, 638, 314
- Drążkowska, J., Li, S., Birnstiel, T., Stammer, S. M., & Li, H. 2019, *ApJ*, 885, 91
- Duval, S. E., Bosman, A. D., & Bergin, E. A. 2022, *ApJ*, 934, L25
- Ehrig, R., Nowak, U., Oeverdieck, L., & Deuffhard, P. 1999, in *High Performance Scientific and Engineering Computing*, ed. M. Griebel, D. E. Keyes, R. M. Nieminen, D. Roose, T. Schlick, H.-J. Bungartz, F. Durst, & C. Zenger, Vol. 8 (Berlin, Heidelberg: Springer Berlin Heidelberg), 233–241, series Title: Lecture Notes in Computational Science and Engineering
- Facchini, S., Birnstiel, T., Bruderer, S., & van Dishoeck, E. F. 2017, *A&A*, 605, A16, publisher: EDP ADS Bibcode: 2017A&A...605A..16F
- Faure, A. & Josselin, E. 2008, *A&A*, 492, 257
- France, K., Schindhelm, R., Bergin, E. A., Roueff, E., & Abgrall, H. 2014, *ApJ*, 784, 127
- Gasman, D., Temmink, M., van Dishoeck, E. F., et al. 2025, *A&A*, 694, A147
- Gasman, D., van Dishoeck, E. F., Grant, S. L., et al. 2023, *A&A*, 679, A117
- Glassgold, A. E., Meijerink, R., & Najita, J. R. 2009, *ApJ*, 701, 142
- Grant, S. L., Temmink, M., van Dishoeck, E. F., et al. 2025, *A&A*, 702, A126
- Grant, S. L., van Dishoeck, E. F., Tabone, B., et al. 2023, *ApJ*, 947, L6
- Greenwood, A. J., Kamp, I., Waters, L. B. F. M., Woitke, P., & Thi, W.-F. 2019a, *A&A*, 626, A6
- Greenwood, A. J., Kamp, I., Waters, L. B. F. M., Woitke, P., & Thi, W.-F. 2019b, *A&A*, 631, A81
- Güttler, C., Blum, J., Zsom, A., Ormel, C. W., & Dullemond, C. P. 2010, *A&A*, 513, A56
- Harada, N., Herbst, E., & Wakelam, V. 2010, *ApJ*, 721, 1570
- Heays, A. N., Bosman, A. D., & van Dishoeck, E. F. 2017, *A&A*, 602, A105
- Henning, T., Kamp, I., Samland, M., et al. 2024, *Publications of the Astronomical Society of the Pacific*, 136, 054302
- Hickson, K. M., Loison, J.-C., Nunez-Reyes, D., & Mereau, R. 2016, *arXiv e-prints*, arXiv:1608.08877
- Horne, K. & Marsh, T. R. 1986, *MNRAS*, 218, 761
- Houge, A., Johansen, A., Bergin, E., et al. 2025a, *A&A*, 699, A227
- Houge, A., Krijt, S., Banzatti, A., et al. 2025b, *MNRAS*, 537, 691
- Hrodmarsson, H. R. & van Dishoeck, E. F. 2023, *A&A*, 675, A25
- Husain, D. & Kirsch, L. J. 1971, *Trans. Faraday Soc.*, 67, 2025
- Hébrard, E., Dobrijevic, M., Pernot, P., et al. 2009, *The Journal of Physical Chemistry A*, 113, 11227
- Jonkheid, B., Kamp, I., Augereau, J.-C., & van Dishoeck, E. F. 2006, *A&A*, 453, 163
- Kaeufer, T., Woitke, P., Min, M., Kamp, I., & Pinte, C. 2023, *A&A*, 672, A30
- Kalyaan, A., Pinilla, P., Krijt, S., et al. 2023, *ApJ*, 954, 66
- Kalyaan, A., Pinilla, P., Krijt, S., Mulders, G. D., & Banzatti, A. 2021, *ApJ*, 921, 84
- Kamp, I., Henning, T., Arabhavi, A. M., et al. 2023, *Faraday Discussions*, 245, 112
- Kamp, I., Thi, W.-F., Woitke, P., et al. 2017, *A&A*, 607, A41
- Kanwar, J., Kamp, I., Jang, H., et al. 2024, *A&A*, 689, A231
- Kanwar, J., Kamp, I., Woitke, P., et al. 2024, *A&A*, 681, A22
- Kanwar, J., Kamp, I., Woitke, P., et al. 2026, *A&A*, 705, A222
- Kanwar, J., Woitke, P., Kamp, I., Rimmer, P., & Helling, C. 2025, *A&A*, 698, A294
- Krijt, S., Banzatti, A., Zhang, K., et al. 2025, *ApJ*, 990, L72
- Krijt, S., Bosman, A. D., Zhang, K., et al. 2020, *ApJ*, 899, 134
- Krijt, S., Ciesla, F. J., & Bergin, E. A. 2016, *ApJ*, 833, 285
- Kruse, T. & Roth, P. 1997, *The Journal of Physical Chemistry A*, 101, 2138
- Lenzuni, P., Gail, H.-P., & Henning, T. 1995, *ApJ*, 447, 848
- Li, J., Xie, C., & Guo, H. 2017, *Physical Chemistry Chemical Physics (Incorporating Faraday Transactions)*, 19, 23280
- Ligterink, N. F. W., Kipfer, K. A., & Gavino, S. 2024, *A&A*, 687, A224
- Loison, J.-C., Agúndez, M., Wakelam, V., et al. 2017, *MNRAS*, 470, 4075
- Lubow, S. H. & D'Angelo, G. 2006, *ApJ*, 641, 526
- Lynden-Bell, D. & Pringle, J. E. 1974, *MNRAS*, 168, 603
- Madhusudhan, N., Agúndez, M., Moses, J. I., & Hu, Y. 2016, *Space Science Reviews*, 205, 285
- Mah, J., Bitsch, B., Pascucci, I., & Henning, T. 2023, *A&A*, 677, L7
- Mathis, J. S., Rumpl, W., & Nordsieck, K. H. 1977, *ApJ*, 217, 425
- Mayor, M. & Queloz, D. 1995, *Nature*, 378, 355
- McElroy, D., Walsh, C., Markwick, A. J., et al. 2013, *A&A*, 550, A36
- Meijerink, R., Pontoppidan, K. M., Blake, G. A., Poelman, D. R., & Dullemond, C. P. 2009, *ApJ*, 704, 1471
- Millar, T. J., Walsh, C., Van De Sande, M., & Markwick, A. J. 2023, *A&A*
- Miotello, A., Bruderer, S., & van Dishoeck, E. F. 2014, *A&A*, 572, A96
- Miotello, A., Facchini, S., van Dishoeck, E. F., et al. 2019, *A&A*, 631, A69
- Miotello, A., van Dishoeck, E. F., Williams, J. P., et al. 2017, *A&A*, 599, A113
- Morales-Calderón, M., Jang, H., Arabhavi, A. M., et al. 2025, *A&A*, 703, A18
- Najita, J. R., Ádámkóvics, M., & Glassgold, A. E. 2011, *ApJ*, 743, 147
- Najita, J. R., Carr, J. S., Pontoppidan, K. M., et al. 2013, *ApJ*, 766, 134
- Notsu, S., van Dishoeck, E. F., Walsh, C., Bosman, A. D., & Nomura, H. 2021, *A&A*, 650, A180
- Öberg, K. I. & Bergin, E. A. 2021, *Phys. Rep.*, 893, 1
- Öberg, K. I., Guzmán, V. V., Walsh, C., et al. 2021, *ApJS*, 257, 1
- Öberg, K. I., Murray-Clay, R., & Bergin, E. A. 2011, *ApJ*, 743, L16
- O'Donovan, B. & Bitsch, B. 2026, *A&A*, 706, A30
- Pasternack, L., Pitts, W., & McDonald, J. 1981, *Chemical Physics*, 57, 19
- Pinilla, P., Birnstiel, T., Ricci, L., et al. 2012, *A&A*, 538, A114
- Pitts, W. M., Pasternack, L., & McDonald, J. 1982, *Chemical Physics*, 68, 417
- Pontoppidan, K. M., Salyk, C., Blake, G. A., et al. 2010, *ApJ*, 720, 887
- Ribas, A., Espaillat, C. C., Macías, E., & Sarro, L. M. 2020, *A&A*, 642, A171
- Rice, W. K. M., Armitage, P. J., Wood, K., & Lodato, G. 2006, *MNRAS*, 373, 1619
- Riols, A. & Lesur, G. 2018, *A&A*, 617, A117
- Salyk, C., Pontoppidan, K. M., Blake, G. A., et al. 2008, *ApJ*, 676, L49
- Salyk, C., Pontoppidan, K. M., Blake, G. A., Najita, J. R., & Carr, J. S. 2011, *ApJ*, 731, 130
- Schindhelm, R., France, K., Herczeg, G. J., et al. 2012, *ApJ*, 756, L23
- Schneider, A. D. & Bitsch, B. 2021, *A&A*, 654, A71
- Schwarz, K. R., Henning, T., Christiaens, V., et al. 2024, *ApJ*, 962, 8
- Sellek, A. D. & van Dishoeck, E. F. 2025, *A&A*, 701, A239
- Sellek, A. D., Vlasblom, M., & van Dishoeck, E. F. 2025, *A&A*, 694, A79
- Silva, R., Gichuhi, W. K., Huang, C., et al. 2008, *Proceedings of the National Academy of Science*, 105, 12713
- Stammer, S. M., Lichtenberg, T., Drążkowska, J., & Birnstiel, T. 2023, *A&A*, 670, L5
- Sturm, J. A., McClure, M. K., Harsono, D., et al. 2022, *A&A*, 660, A126
- Tabone, B., Bettoni, G., van Dishoeck, E. F., et al. 2023, *Nature Astronomy*, 7, 805
- Tabone, B., Temmink, M., Waters, L. B. F. M., et al. 2026, *arXiv e-prints*, arXiv:2604.21803
- Tabone, B., van Dishoeck, E. F., & Black, J. H. 2024, *A&A*, 691, A11
- Tazaki, R. & Dominik, C. 2022, *A&A*, 663, A57
- Temmink, M., Sellek, A. D., Gasman, D., et al. 2025, *A&A*, 699, A134
- Temmink, M., van Dishoeck, E. F., Grant, S. L., et al. 2024, *A&A*, 686, A117
- Tinacci, L., Ferrada-Chamorro, S., Ceccarelli, C., et al. 2023, *ApJS*, 266, 38
- van Dishoeck, E. F. & Black, J. H. 1982, *ApJ*, 258, 533
- van Dishoeck, E. F., Grant, S., Tabone, B., et al. 2023, *Faraday Discussions*, 245, 52
- van Dishoeck, E. F., Herbst, E., & Neufeld, D. A. 2013, *Chemical Reviews*, 113, 9043
- van Hemert, M. & van Dishoeck, E. 2008, *Chemical Physics*, 343, 292
- Visser, R., Bruderer, S., Cazzoletti, P., et al. 2018, *A&A*, 615, A75
- Vlasblom, M., Temmink, M., Grant, S. L., et al. 2025, *A&A*, 693, A278
- Vlasblom, M., van Dishoeck, E. F., Tabone, B., & Bruderer, S. 2024, *A&A*, 682, A91

- Wakelam, V., Gratier, P., Loison, J.-C., et al. 2024, A&A, 689, A63
- Walsh, C., Nomura, H., & van Dishoeck, E. 2015, A&A, 582, A88
- Weber, P., Benítez-Llambay, P., Gressel, O., Krapp, L., & Pessah, M. E. 2018, ApJ, 854, 153
- Weidenschilling, S. J. 1977, MNRAS, 180, 57
- Weingartner, J. C. & Draine, B. T. 2001, ApJ, 548, 296
- Williams, J., Krijt, S., Bitsch, B., Houge, A., & Bergner, J. 2025, MNRAS, 544, 3562
- Woitke, P., Arabhavi, A. M., Kamp, I., & Thi, W.-F. 2022, A&A, 668, A164
- Woitke, P., Kamp, I., & Thi, W.-F. 2009, A&A, 501, 383
- Woitke, P., Min, M., Pinte, C., et al. 2016, A&A, 586, A103
- Woitke, P., Min, M., Thi, W.-F., et al. 2018, A&A, 618, A57
- Woitke, P., Thi, W.-F., Arabhavi, A. M., et al. 2024, A&A, 683, A219
- Wolfire, M. G., McKee, C. F., Hollenbach, D., & Tielens, A. G. G. M. 2003, ApJ, 587, 278
- Zhu, Z., Nelson, R. P., Dong, R., Espaillat, C., & Hartmann, L. 2012, ApJ, 755, 6
- Zsom, A., Ormel, C. W., Güttler, C., Blum, J., & Dullemond, C. P. 2010, A&A, 513, A57

Appendix A: UV shielding

Appendix A.1: New implementation

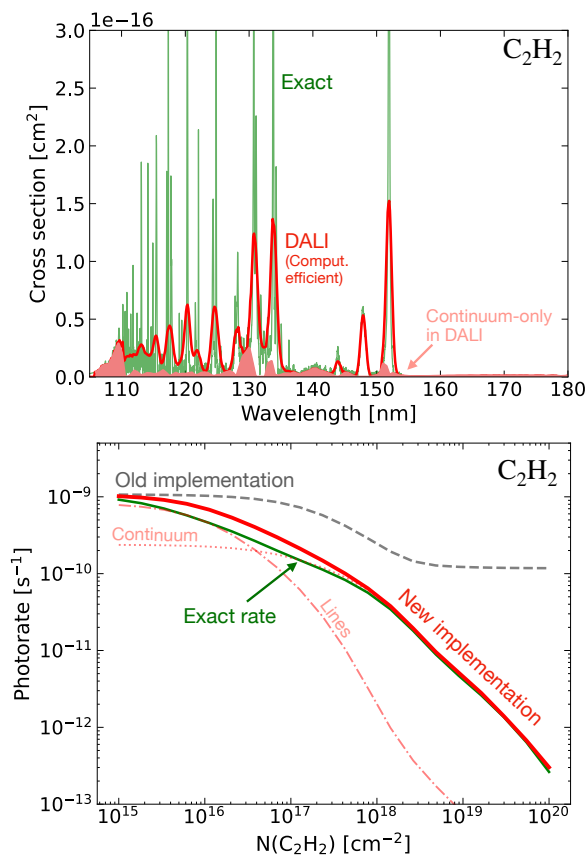


Fig. A.1. Top panel: Difference between the exact cross section of C_2H_2 (in green) and used in DALI (red, corresponding to the ‘computational efficiency’ format in the Leiden Database). The light red curve shows only the continuum part of the cross section in the computational efficiency format. Bottom panel: Improvement of the UV shielding with the new implementation. The green line shows the exact photodissociation rate (computed with the exact cross section). Continuum (dashed red line) and lines (dashed-dotted line) correspond respectively to the contribution of the dissociation in the continuum (i.e light red curve in the top panel) and in the lines.

The results from the new implementation of the UV shielding are shown on Fig. A.1. The exact cross section of C_2H_2 is shown in green in the top panel (Heays et al. 2017). Since it is highly wavelength dependent with many narrow lines, DALI uses the ‘computational efficiency’ format in the Leiden Database (red in the top panel Fig. A.1). This format splits the cross section in two parts: lines (if FWHM < 1 nm) and continuum. In the top panel of the Fig. A.1, the continuum cross section is highlighted by the light red curve, while the rest of the DALI cross section corresponds to the contribution of the lines. This approach significantly reduces the number of wavelength points (< 500 for the continuum) which avoids very fine sampling of the radiative field. The bottom panel of the Fig. A.1 shows how well this approximation agrees with the exact photodissociation rate. As the column density of C_2H_2 increases, the photodissociation rate drops because the molecule protects itself. The previous implementation, which considered only the continuum cross section (light red in the top panel), is shown as dashed grey line. The new implementation is shown as red

solid line, for which both the ‘Continuum’ and the ‘Lines’ cross sections (see top panel) are taken into account:

$$k = \int \sigma^{cont}(\lambda) I(\lambda) d\lambda + \sum_{lines} \sigma^{int} I(\lambda_0) \times \alpha(\sigma^{int}, N) \quad (A.1)$$

The first term corresponds to the dissociation in the continuum, with σ^{cont} the continuum cross section (in light red the top panel, and illustrated with dotted line ‘Continuum’ in the bottom panel). The second term corresponds to the dissociation in the lines, with the integrated cross section σ^{int} (illustrated in the bottom panel with the dashed-dotted line ‘Lines’). The attenuation factor in the lines, $\alpha(\sigma^{int}, N)$ can be expressed as:

$$\alpha = \int \frac{1}{\sqrt{\pi}} e^{-y^2} e^{-\frac{\kappa}{\sqrt{\pi}} e^{-y^2}} dy \quad (A.2)$$

where $\kappa = \sigma^{int} N / \Delta\lambda \sqrt{2}$. The FWHM of the Gaussian is set to 1 nm ($\Delta\lambda = \text{FWHM} / 2.355$) and N is the column density of the absorbing species.

The difference observed between the old and the new implementation at low column densities ($N_{C_2H_2} < 10^{17} \text{ cm}^{-2}$) is due to the photodissociation in the lines: as mentioned earlier in section 2.2.1, self-shielding appears first in the lines since cross sections peak ~ 10 - 100 times above the continuum. This effect is highlighted by the light red dashed-dotted line that drops first, very quickly. This also reflects the importance of photodissociation in lines, by a drop of ~ 1 order of magnitude at column densities around $N = 5 \times 10^{17} \text{ cm}^{-2}$. At higher column densities, the continuum begins to attenuate the UV field (red dotted line). The old implementation reaches a plateau and strongly overestimates the photodissociation rate compared to the exact rate (green). Indeed, C_2H_2 could still be photodissociated in the lines since their shielding was not taken into account. The new implementation gives a much better estimation at high column densities, almost perfectly matching the exact rate. In the case of C_2H_2 , the slight overestimation of the new implementation at $N \sim 10^{16} \text{ cm}^{-2}$ reflects the limit of approximating narrow lines (< 1 nm) to much wider lines (FWHM = 1 nm), the latter peaking at much smaller values to conserve the total energy absorbed.

Appendix A.2: Mutual shielding

The Fig. A.2 shows the ability of molecules to protect themselves (self-shielding) and protect other molecules (mutual shielding). The top panel shows the evolution of photodissociation rates of molecules with H_2O , C_2H_2 and CH_4 shielding the gas. For the bottom panel, HCN, CO_2 and C_3 are shielding. The attenuation seen in these figures is only due to gas absorption, dust being excluded. The figure highlights the special role played by water, being the most efficient molecule in protecting other species. We can note that C_3 is also particularly efficient, having a broad cross section as well. However, the specific width of the cross section of C_3 was assumed from the work of van Hemert & van Dishoeck (2008) (see Section 4.3.24. in Heays et al. 2017), but it has never been measured experimentally. Its ability to mutually shield thus relies on this assumption. C_2H_2 can protect water only at high column densities. Regarding HCN, CO_2 and CH_4 , they are not relevant in the mutual shielding. NH_3 is relatively unaffected, even with water shielding due to a cross section extending up to 225 nm (Heays et al. 2017).

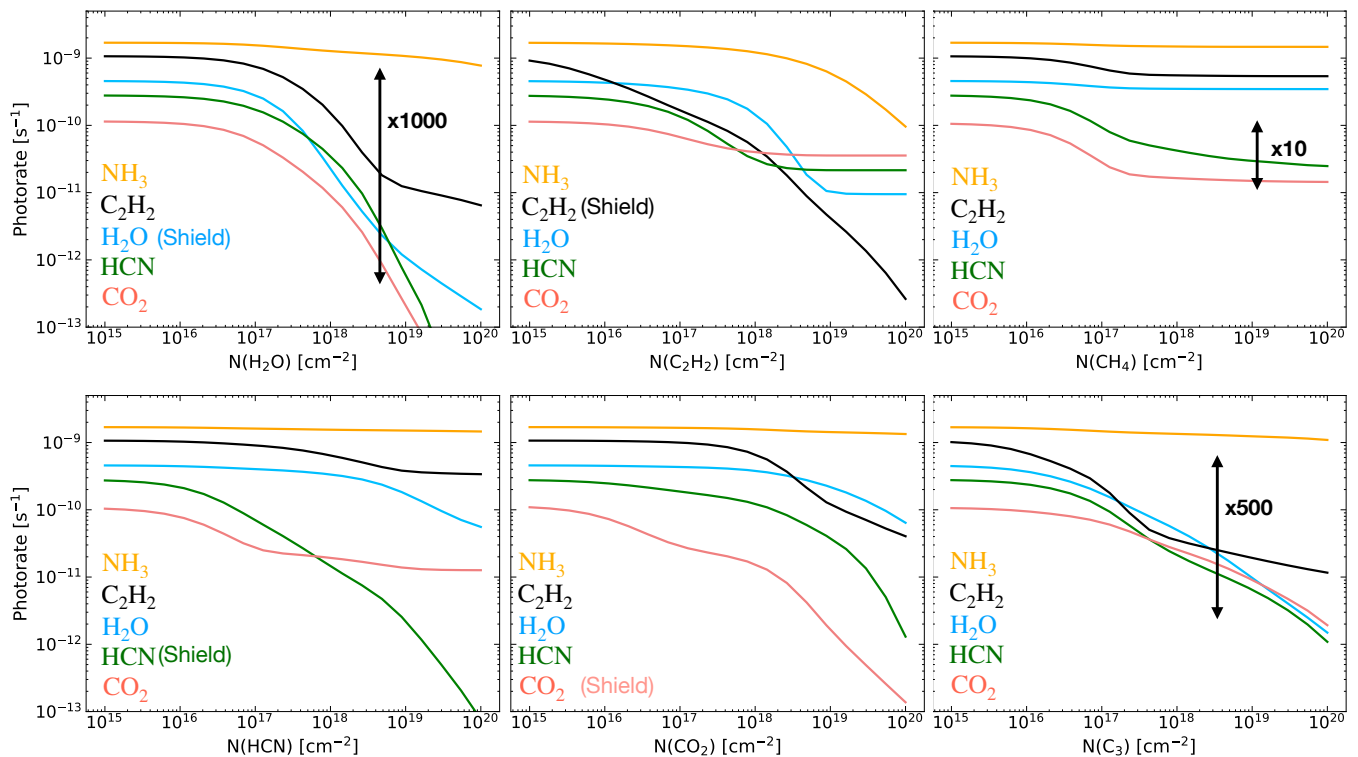


Fig. A.2. UV shielding efficiency of 6 abundant molecules: H_2O , C_2H_2 , CH_4 (top panel) and HCN , CO_2 , C_3 (bottom panel). H_2O and C_3 are powerful molecules to shield the gas, by reducing the photodissociation rate of most of the molecules by 2 to 3 orders of magnitude. On the contrary, CH_4 or HCN are not relevant for the mutual shielding. NH_3 is relatively unaffected by molecular shielding, as its cross section extends up to 225 nm.

Table A.1. Species included in the network with $c\text{-C}_3\text{H}_2$ UV cross section.

nb C	Species
1	CH_3^+
2	C_2^+ , C_2N
3	CH_2CCH_2 , CH_3CCH , CH_3CHCH_2 , C_3H_5
4	CH_2CHCCH , C_4H_3 , $\text{CH}_2\text{CHCHCH}_2$, C_4H_2^a
5	C_3CCH , C_5 , C_5H_2 , C_5H_5 , C_5H_6 , $\text{CH}_3\text{C}_4\text{H}$, $\text{H}_2\text{CCCHCCH}$, C_3HCCH

^(a) C_4H_2 has the C_4H cross section.

Appendix A.3: Species with $c\text{-C}_3\text{H}_2$ cross section

Several species added to the network do not have an available UV cross section in the Leiden Database. For these species, we arbitrarily choose the $c\text{-C}_3\text{H}_2$ UV cross section. The list of species for which the $c\text{-C}_3\text{H}_2$ cross section is used to compute the photodissociation rate is in Table A.1. The $c\text{-C}_3\text{H}_2$ cross section has a line at 250 nm, which means that these hydrocarbons can still be photodissociated in a region shielded by water.

For C_4H_2 , we choose the C_4H cross section as it should be more appropriate. Indeed, the dissociation of C_4H_2 leads to C_2H and C_4H , which are very similar to the dissociation fragments of C_4H (C_2 and C_4). In addition, [Silva et al. \(2008\)](#) found that the dissociation rate of C_4H_2 is negligible at $\lambda > 180$ nm, as is that of C_4H .

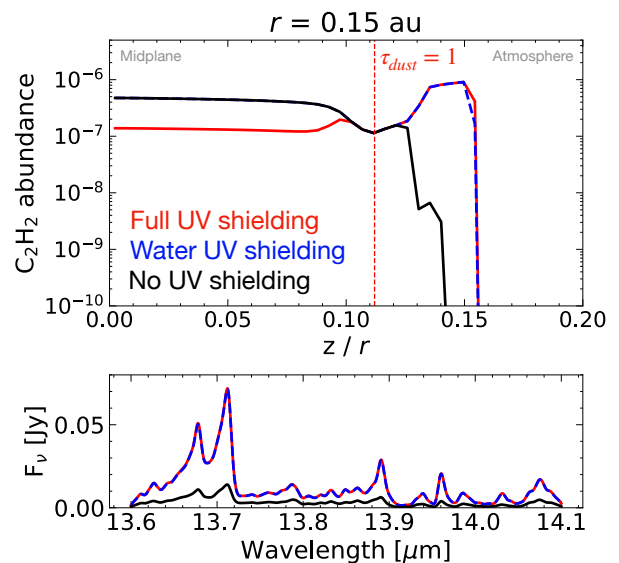


Fig. A.3. Top panel: Vertical cut at $r = 0.15$ au showing the abundance of acetylene when there is no UV shielding by the gas (black), water UV shielding (blue), or the 12 species mentioned in Sect. 2.2.1 (red). Bottom panel: C_2H_2 spectrum for these different UV shielding prescriptions.

Appendix A.4: Effect of UV shielding on C_2H_2

The Fig. A.3 shows the difference between no UV shielding by the gas (in black) and water UV shielding (in dashed blue). Acetylene is 4 orders of magnitude more abundant where

Table B.1. Initial abundances for the fiducial model. Adopted from Bruderer et al. (2012).

Element	Number fraction
H	1.00
He	7.59e-2
C	1.35e-4
N	2.14e-5
O	2.88e-4
Mg	4.17e-7
Si	7.94e-6
S	1.91e-6
Fe	4.27e-7

it emits, increasing the emission of the Q -branch at $13.7 \mu\text{m}$ by a factor 5. However, the red line shows that when we include the shielding from other abundant species (S, Fe, H_2O , OH, CO_2 , HCN, CN, C_2H_2 , C_3 , C_2H_4 , CH_4 , C_2H_6), the difference is not significant for a solar C/O. It shows that it is indeed the water UV shielding that determines the position of the molecular layer in the inner disk.

Appendix B: Chemistry

Appendix B.1: Initial abundances

Table B.1 indicates the initial elemental abundances for the fiducial model. For the model grid, we vary the C/O ratio by keeping O/H constant and changing C/H. For enhanced O/H, the O/H ratio is increased by a factor 10, and we vary the C/H ratio to match the desired C/O ratio. We follow the same procedure for the depleted grid, by reducing the O/H ratio by a factor 10.

Appendix B.2: New species

Table B.2 lists all the species added to the chemical network. It includes all hydrocarbons (C_xH_y) available in UMIST with less than 6 atoms of carbon.

Appendix B.3: Updated endothermicity for KIDA reactions

Table B.3 indicates the list of reactions included in our chemical network with the corrected endothermicity from Tinacci et al. (2023). Table B.4 lists all the reactions that have not been included in the chemical network because the reaction enthalpy is above the threshold of $\Delta H_r > 12,000 \text{ K}$ after the correction of Tinacci et al. (2023). These two tables show that carbon chains with 3 carbons and 5 carbons are much less reactive than expected. In particular, the correction makes C_3 much more abundant by suppressing its reactivity with H_2 .

Appendix B.4: Focus on $\text{C}_n + \text{H}_2$

The reaction $\text{H}_2 + \text{C}_2 \rightarrow \text{C}_2\text{H} + \text{H}$ is crucial for the final abundance of C_2H_2 in the inner disk, since the reaction $\text{H}_2 + \text{C}_2\text{H} \rightarrow \text{C}_2\text{H}_2 + \text{H}$ is very fast. However, NIST and KIDA databases give an inconsistent rate coefficient for this reaction. It does not exist in UMIST (RATE22 Millar et al. 2023), possibly explaining why this reaction has been neglected in studies based on UMIST (Walsh et al. 2015). KIDA reports an activation barrier of 1420 K (Harada et al. 2010), while NIST places this activation energy at 4000 K. In the literature, two values of the activation barrier have been proposed. Pitts et al. (1982) found an

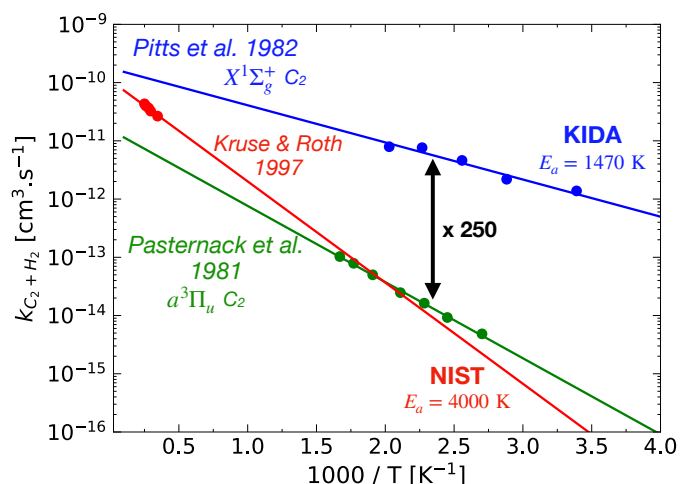


Fig. B.1. Inconsistency of the rate coefficient of $\text{H}_2 + \text{C}_2 \rightarrow \text{C}_2\text{H} + \text{H}$ between KIDA (blue) and NIST (red) database, coming from a different initial state of C_2 : the rate coefficient of NIST (Kruse & Roth 1997) corresponds to the triplet state $a^3\Pi_u$ according to Pasternack et al. (1981).

activation energy of 1470 K, based on laser experiments at room temperature, while Kruse & Roth (1997) used shock experiments to find that this activation energy should be at 4000 K, for a temperature between 2500 and 4500 K. By extrapolating this latter rate coefficient, we found that it is consistent with the results of Pasternack et al. (1981), but inconsistent with the values from Pitts et al. (1982) tabulated in KIDA. In fact, this disagreement comes from different initial states of C_2 when it reacts with H_2 (van Dishoeck & Black 1982). The measurements done by Pitts et al. (1982) are related to the singlet $X^1\Sigma_g^+$ state of C_2 (ground state) from which the reaction proceeds very fast. In contrast, Pasternack et al. (1981) measured it for the metastable triplet state $a^3\Pi_u$ of C_2 and found an activation energy of $E_a = 3000 \text{ K}$, which is consistent with the value adopted in NIST and found by Kruse & Roth (1997) (see Fig. B.1). In inner disk conditions, we see no reason why C_2 would only be in his metastable state, so we decide to consider the rate coefficient with the ground state ($E_a = 1500 \text{ K}$) in the chemical network. To verify the activation energy found experimentally by Pitts et al. (1982), M. van Hemert (2025, private communication) performed quantum calculations (multireference configuration interaction MRCI) and estimated an activation barrier in good agreement with the value of Pitts et al. (1982). Therefore, we add in our network the rate coefficient found by Pitts et al. (1982), which was used in Harada et al. (2010) and available in the KIDA database.

Extending these results to longer pure carbon chains (C_n , $n > 2$), KIDA, following Harada et al. (2010), uses the same rate coefficient as for C_2 . Similarly to C_2 , the reaction with C_4 is exothermic, so this assumption seems reasonable. However, only considering the reaction enthalpy with C_3 and C_5 , Tinacci et al. (2023) showed that they are much less reactive with H_2 (14287 K and 9780 K). To go further, this might suggest that pure carbon chains with an even number of carbon are much more reactive than those with an odd number of carbon.

Appendix B.5: The reaction $\text{C} + \text{H}_2\text{O}$

The reaction $\text{C} + \text{H}_2\text{O} \rightarrow \text{HCO} + \text{H}$ can strongly reduce the abundance of hydrocarbons by putting the carbon back to CO (HCO leading to CO). Its reaction rate is known to be very low, with an upper limit of $k < 3.6 \times 10^{-13} \text{ cm}^3 \cdot \text{s}^{-1}$ (Husain & Kirschn

Table B.2. New species added to the chemical network.

2C	3C	4C	5C
	C ₃ , C ₃ ⁺	C ₄ , C ₄ ⁺	C ₅ , C ₅ ⁺
	C ₃ H, C ₃ H ⁺	C ₄ H, C ₄ H ⁺	C ₃ CCH, C ₅ H, C ₃ CCH ⁺ , C ₅ H ⁺
	C ₃ H ₂ , H ₂ CCC, C ₃ H ₃ ⁺	C ₄ H ₂ , C ₄ H ₂ ⁺	C ₅ H ₂ , C ₃ HCCH, C ₅ H ₃ ⁺ , C ₃ HCCH ⁺ , C ₃ CCH ₂ ⁺
	CH ₂ CCH, H ₂ CCCH ⁺ , C ₃ H ₃ ⁺	C ₄ H ₃ , C ₄ H ₃ ⁺	C ₃ HCCH ₂ ⁺ , C ₅ H ₃ ⁺
C ₂ H ₄ , C ₂ H ₄ ⁺	CH ₂ CCH ₂ , CH ₃ CCH, C ₃ H ₄ ⁺	CH ₂ CHCCH, C ₄ H ₄ ⁺	CH ₃ C ₄ H, H ₂ CCCHCCH, CH ₃ C ₄ H ⁺ , C ₅ H ₄ ⁺
C ₂ H ₅ , C ₂ H ₅ ⁺	C ₃ H ₅ , CH ₂ CCH ₃ ⁺ , C ₃ H ₅ ⁺	C ₄ H ₅ ⁺ , CH ₂ CHCCH ₂ ⁺	C ₅ H ₅ , C ₅ H ₅ ⁺
CH ₃ CH ₃ , CH ₃ CH ₃ ⁺	CH ₃ CHCH ₂ , C ₃ H ₆ ⁺	CH ₂ CHCHCH ₂	C ₅ H ₆ , C ₅ H ₆ ⁺
C ₂ H ₇ ⁺	C ₃ H ₇ ⁺	C ₄ H ₇ ⁺	C ₅ H ₇ ⁺

Table B.3. Reactions from KIDA corrected with the endothermicity found by Tinacci et al. (2023).

Reaction	α [cm ³ .s ⁻¹]	β	γ_{KIDA} [K]	$\gamma_{corrected}$ [K]
C ₂ H ₃ + CH ₃ ⁺ → H ₂ CCH ⁺ + H ₂ + H	9.50 × 10 ⁻¹¹	-0.5	0.0	1878
CH ₄ + H ₂ CCC → CH ₃ + CH ₂ CCH	5.90 × 10 ⁻¹¹	0.0	0.0	2210
H ₂ + C ₃ H ₂ → H + CH ₂ CCH	3.74 × 10 ⁻¹²	2.0	1740	8766
CH ₂ + C ₄ H ₂ → CH ₃ + C ₄ H	2.16 × 10 ⁻¹¹	0.0	2160	11400
H ₂ + C ₄ H ₂ ⁺ → H + C ₄ H ₃ ⁺	1.00 × 10 ⁻⁹	0.0	2000	5339
H ₂ + C ₅ H → H + C ₅ H ₂	1.14 × 10 ⁻¹¹	0.0	950	9578
H ₂ + C ₅ → H + C ₅ H	1.60 × 10 ⁻¹⁰	0.0	1420	9780

Table B.4. Reactions corrected with the reaction enthalpy found by Tinacci et al. (2023), but not included in the chemical network. The activation barrier ($\gamma_{corrected}$) is above the threshold of 12000 K.

Reaction	α [cm ³ .s ⁻¹]	β	γ_{KIDA} [K]	$\gamma_{corrected}$ [K]
H ₂ + C ₅ H ⁺ → H + C ₅ H ₂ ⁺	1e-17	0.0	0	20421
H ₂ + C ₂ ⁺ → C ₂ H + H ⁺	1.5e-09	0.0	1260	18358
C ₄ H ₂ + C ₃ H ⁺ → C ₂ H + C ₅ H ₃ ⁺	1e-09	0.0	0	24113
CH ₃ + CH ₃ CCH → C ₂ H + CH ₃ CH ₃	8.32e-13	0.0	4430	18587
CH ₃ + C ₄ H ₃ → C ₂ H + C ₃ H ₅	1.2e-10	0.0	0	12037
C ₂ H ₂ + C ₂ H ₅ → C ₂ H + CH ₃ CH ₃	4.5e-13	0.0	11800	16172
H + C ₅ H ₃ ⁺ → H ₂ + C ₅ H ₂ ⁺	7e-10	0.0	700	13558
H ₂ + C ₃ → H + C ₃ H	8e-12	0.0	1420	14287
H + C ₄ H ₂ → C ₂ H + C ₂ H ₂	9.96e-10	0.0	7750	14194
H + C ₅ H ₂ → C ₂ H + H ₂ CCC	4.98e-10	0.0	7750	13973
H ₂ + C ₄ H ₂ → H + C ₄ H ₃	4.91e-10	-0.16	27900	29610

1971, NIST), and might explain why this reaction is missing in UMIST. However, the measurements of Hickson et al. (2016) at low temperature revealed that the reaction rate is much higher than the upper limit of Husain & Kirsch (1971) (see Fig. B.2). This has been interpreted as an efficient quantum tunnelling at low temperature, which allows to cross the activation barrier. The online KIDA database includes this reaction (leading to "Products"), but as noted by Woitke et al. (2024), the rate is unreasonably high and inconsistent with Husain & Kirsch (1971); Hickson et al. (2016). The *ab initio* calculations of Li et al. (2017) confirmed that the rate is indeed low at high temperature (see Fig. B.2), consistent with Husain & Kirsch (1971), which means that tunnelling is not efficient in this regime. We decided to include this reaction in our chemical network by adopting the reaction rate of Hickson et al. (2016) at low temperature and Li et al. (2017) at high temperature (in red Fig. B.2). The reaction rate is uncertain between $T \sim 200 - 500$ K, so we fitted the data points with a modified Arrhenius law for two separate temperature ranges and extrapolated the low temperature rate until 500 K:

$$k(T) = \begin{cases} 1.314 \times 10^{-13} \left(\frac{T}{300}\right)^{-4.394} e^{-112.9/T} & \text{if } T \in [10, 500] \text{ K} \\ 1.502 \times 10^{-15} \left(\frac{T}{300}\right)^{4.522} e^{-125.7/T} & \text{if } T \in [500, 1000] \text{ K} \end{cases}$$

(B.1)

The emission of C₂H₂ is reduced by ~ 30% in the fiducial model, due to a lower abundance around 0.3-0.7 au, where the temperature is below 300 K.

Appendix B.6: Key reactions in KIDA missing in UMIST

The difference up to three orders of magnitude in C₂H₂ abundance between a chemical network based on UMIST+KIDA and based only in UMIST (Fig. 7) can be explained by 7 key reactions in KIDA, listed in the table B.5. Five of these seven reactions are H-abstractions revealing the crucial role of H₂ in the formation of C₂H₂. The rate coefficients of C_n + H₂ and C_nH + H₂ are the same as C₂ + H₂ and C₂H + H (Harada et al. 2010).

Appendix C: Line overlap

Fig. C.1 shows the result of including the line overlap for the raytracing of C₂H₂ (in red). It does not significantly reduce acetylene emission in the Q-branch. The presence of the pseudo-continuum near $\lambda = 13.74 \mu\text{m}$ reveals that there is still optically

Table B.5. Key reactions from KIDA explaining the difference between the chemical network based on UMIST+KIDA and UMIST only. Most of these reactions are H-abstractions, revealing the crucial role of H₂ in the formation of acetylene.

Reaction	α [cm ³ .s ⁻¹]	β	γ [K]	Reference
C ₂ + H ₂ → C ₂ H + H	1.60e-10	0.0	1420	Pitts et al. (1982); Harada et al. (2010)
C ₃ H + H ₂ → C ₃ H ₂ + H	1.14e-11	0.0	950	Harada et al. (2010)
H ₂ CCC + H ₂ → CH ₂ CCH + H	3.74e-12	2.0	1740	Harada et al. (2010)
C ₄ + H ₂ → C ₄ H + H	1.60e-10	0.0	1420	Harada et al. (2010)
C ₄ H + H ₂ → C ₄ H ₂ + H	1.14e-11	0.0	950	Harada et al. (2010)
N + CH ₂ CCH → C ₂ H ₂ + HCN	5.00e-11	0.0	0.0	Loison et al. (2017)
C ₄ H ₃ ⁺ + e ⁻ → C ₂ H ₂ + C ₂ H	1.10e-07	0.0	0.0	Loison et al. (2017)

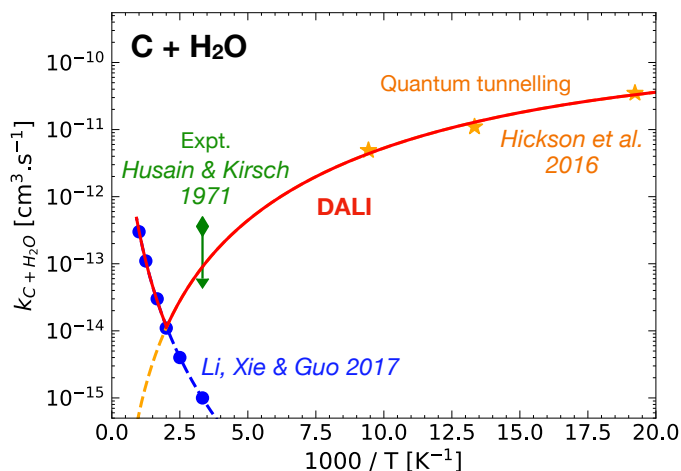


Fig. B.2. Rate coefficient of the reaction C+H₂O → HCO+H adopted in this work (red). This rate is in agreement with the upper limit of Husain & Kirsch (1971), the *ab initio* calculations of Li et al. (2017) and the measurements of Hickson et al. (2016).

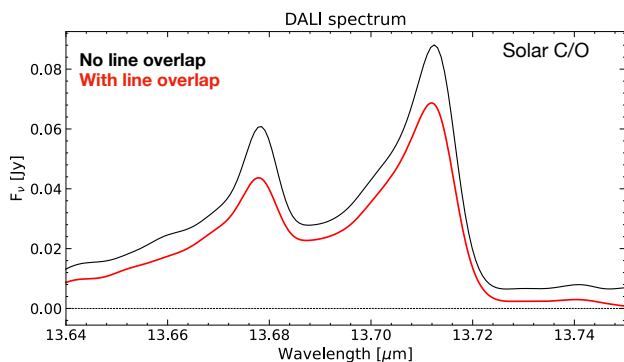


Fig. C.1. DALI spectrum of the Q-branch of C₂H₂ at 13.7 μm without line overlap (in black) and with line overlap (in red). With a solar C/O, the difference is not significant in the Q-branch (factor 1.5) whereas it is more pronounced in the pseudo-continuum (factor ~ 4 near λ = 13.74 μm).

thick emission of C₂H₂, originating from the deepest layers in its emitting regions.

Appendix D: Depleted O/H grid

Figure D.1 presents the C₂H₂ and H₂O emissions obtained with the depleted O/H grid (10 times less oxygen than the fiducial grid) to mimic late times in protoplanetary disks, where the water vapor is advected onto the star and the metal-poor gas

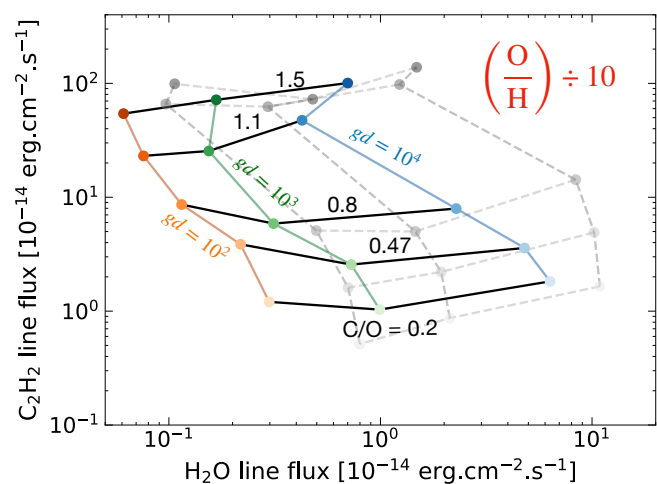


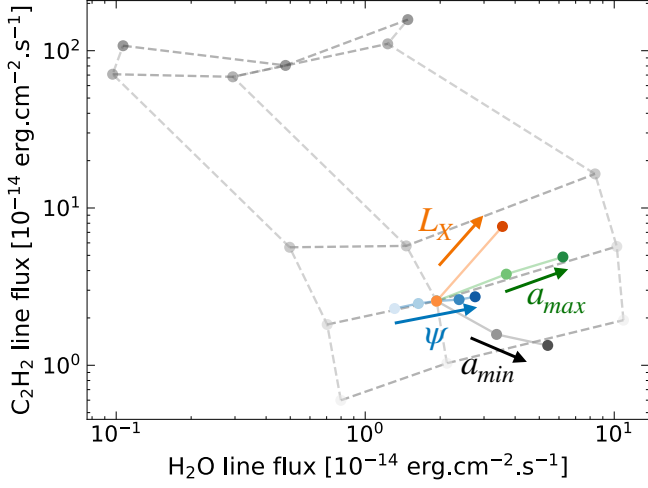
Fig. D.1. Same figure as Fig. 4-b showing the depleted O/H grid.

from the outer disk is reaching the inner regions (Mah et al. 2023; Sellek & van Dishoeck 2025). The decrease in oxygen, which enhances C₂H₂ formation, is balanced by a water shielding becoming less effective, leading to an increase of a factor of 2 in acetylene emission. The effect of the oxygen depletion is stronger for H₂O, shifting the grid to the left side (small H₂O emission) rather than top-left.

Appendix E: Other parameters

Fig. E.1 presents the results for the other parameters explored in this work: the minimum and maximum grain size a_{min} and a_{max} , the flaring angle ψ and the X-ray luminosity L_X . As mentioned in Sect. 3.2.2, increasing a_{min} lowers the opacity in the upper atmosphere, pushing deeper the molecular emitting layers, but keeping the dust emitting layer the same. It reduces C₂H₂ emission as less acetylene is above the $\tau_{dust} = 1$ surface. Water is less affected by the dust continuum as it emits higher up. Pushing its emission into denser layers increases its emission. An increase of 6 orders of magnitude in the X-ray luminosity increases C₂H₂ and H₂O emission by only a factor of 3, showing that these two molecules are not sensitive to X-rays. In particular, it confirms that X-rays are important for both the formation and destruction of C₂H₂, thus canceling their effect on C₂H₂ emission.

Fig. E.2 shows the evolution of the line flux ratio C₂H₂/H₂O with these parameters (a_{min} , a_{max} , ψ , L_X). Considering the two-orders-of-magnitude variation in the observed C₂H₂/H₂O line flux ratio (Grant et al. 2025), these parameters can be considered irrelevant compared to C/O, O/H, or q .



creating a sweetspot where H_2 would be dramatically destroyed. Indeed, in upper layers, C_2 is photodissociated as well, and in deeper layer, C_3 can survive to the UV field. Therefore, this loop is broken for layers above or below this specific region.

Fig. E.1. Same figure as Fig. 4-c showing the impact of a_{min} (black), a_{max} (green), ψ (blue) and L_X (orange). The fiducial grid is shown in grey.

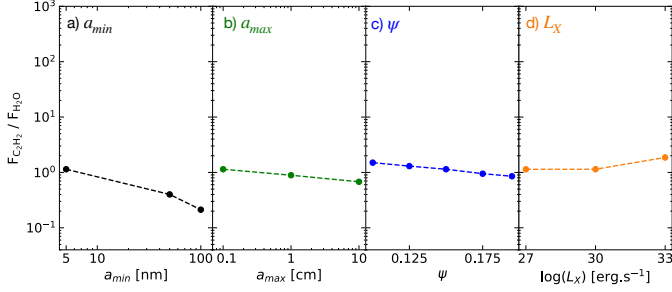


Fig. E.2. Evolution of the line flux ratio $\text{C}_2\text{H}_2/\text{H}_2\text{O}$ with the minimum and maximum grain size, the flaring angle and the X-ray luminosity.

Appendix F: Model with $\text{C}/\text{O} = 1.5$

Fig. F.1-e presents the result for a model with $\text{C}/\text{O} > 1$ (other parameters fixed to the values in the fiducial model). It reveals the dramatic difference with abundances maps of $\text{C}/\text{O} < 1$. C_2H_2 is abundant almost everywhere, and its emitting region is much more extended than with $\text{C}/\text{O} < 1$. On the contrary, water is much less abundant and emits from a smaller region, closer to the star. Figure F.1-d also interestingly shows that the UV field map is significantly different than when the $\text{C}/\text{O} < 1$: this time, C_2H_2 and C_3 absorb the UV photons instead of water with the footprint of C_2H_2 around $r \sim 0.5\text{-}5$ au.

The H/H_2 transition is much higher compared to $\text{C}/\text{O} < 1$, mainly due to the fact that H_2 is no longer destroyed by the warm oxygen chemistry leading to OH and H_2O . However, just above the surface where C_2H_2 becomes abundant, the hydrogen becomes atomic again. In this layer, it is the warm carbon chemistry that consumes H_2 , as it was with oxygen in $\text{C}/\text{O} < 1$. Indeed, H_2 is destroyed by the reactions



Then, C_2H_2 reacts with C to form C_3 . This layer is still strongly irradiated ($G_0 \sim 10^6$), photodissociating C_3 to produce C_2 . Thus, this layer creates a loop between C_2 and C_3 which consumes H_2 . This layer is irradiated enough to photodissociate C_3 but not C_2 ,

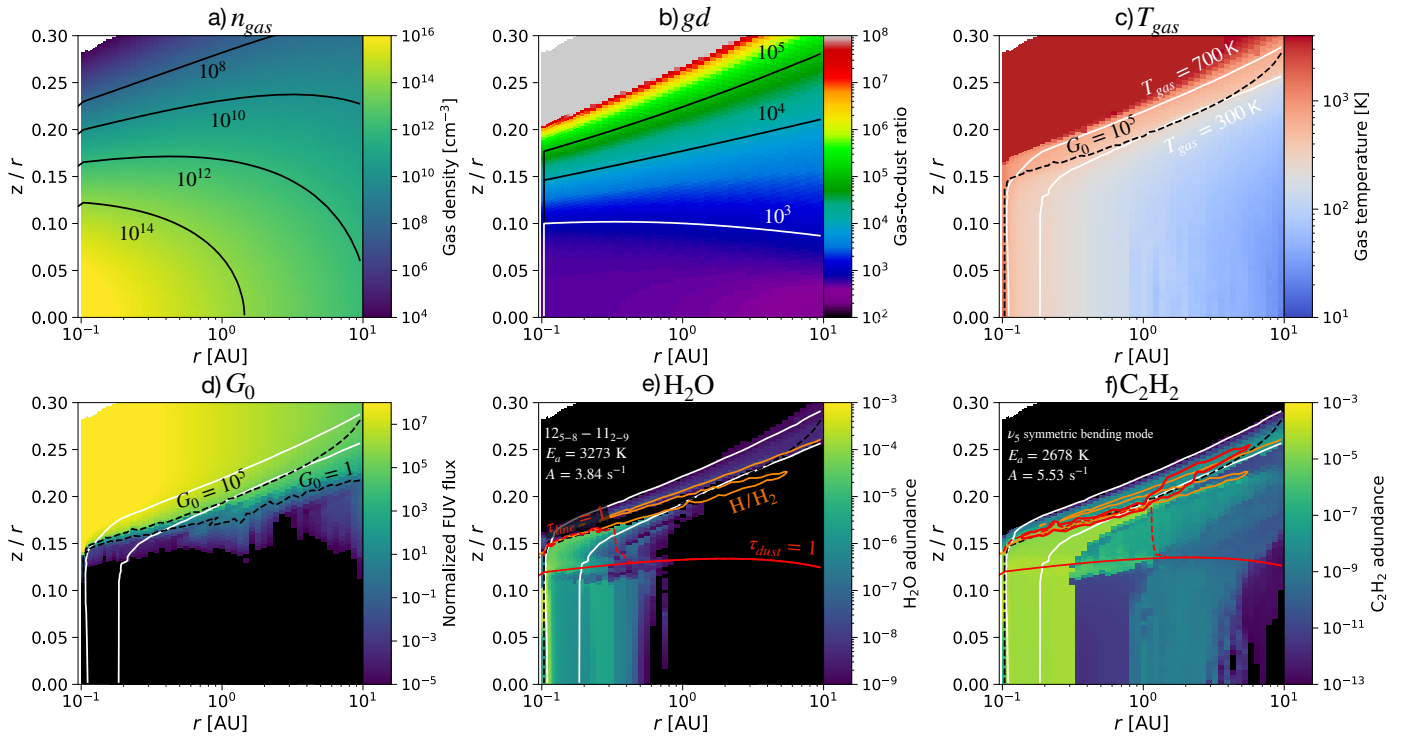


Fig. F.1. Disk structure of the fiducial model but with $C/O = 1.5$. The top panels show the gas density, the gas-to-dust ratio and the gas temperature. The bottom panels present the normalized UV field G_0 (Habing units), the abundance of H_2O and C_2H_2 . The white lines indicate the 300 K and 700 K gas temperature contours. The bottom red solid line shows the dust optically thick surface ($\tau_{dust} = 1$ at $14 \mu m$) while the dashed red line represents the surface where $\tau_{line} = 1$. The red contours correspond to 80% of the total emitting flux. The orange dashed line in the bottom panels indicates the H/H_2 transition, sometimes difficult to distinguish from the black dashed line $G_0 = 10^5$.